An extended rheological map of pāhoehoe - ‘a‘ā transition

F. Di Fiore[1,*], A. Vona[1], S. Kolzenburg[2,3,4], S. Mollo[5,6] and C. Romano[1]

[1] Dipartimento di Scienze, Università degli Studi Roma Tre, L.go San Leonardo Murialdo 1, 00146 Roma, Italy

[2] University at Buffalo, Dep. of Geology, NY 14260-4130 Buffalo, USA

[3] Ludwig-Maximilians - Universität, Dep. of Earth and Environmental Sciences 80333 Munich, Germany

[4] McGill University, Department of Earth and Planetary Sciences H3A 0E8 Montreal, Quebec, Canada

[5] Department of Earth Sciences, Sapienza - University of Rome, P. le Aldo Moro 5, 00185 Roma, Italy

[6] Istituto Nazionale di Geofisica e Vulcanologia - Department Roma 1, Via di Vigna Murata 605, 00143 Roma, Italy

Corresponding author: Fabrizio Di Fiore (fabrizio.difiore@uniroma3.it)

Keywords: Magma and lava viscosity; crystallization kinetics; viscous rupture; lava flows; pāhoehoe – ‘a‘ā transition.

Key Points:

- High-T deformation experiments explore the rheology of a phonotephrite melt under both equilibrium and disequilibrium conditions.
- Crystallization is enhanced by decreasing cooling rate and/or increasing shear rate.
- Rheological data identify and map the pāhoehoe–‘a‘ā transition, controlled by composition, shear rate and cooling path of lavas.

This article has been accepted for publication and undergone full peer review but has not been through the copyediting, typesetting, pagination and proofreading process, which may lead to differences between this version and the Version of Record. Please cite this article as doi: 10.1029/2021JB022035.

Abstract

The pāhoehoe–ʻaʻā morphological transition involves a change in the rheological response of the magmatic suspension from pure viscous to complex rheological behavior, resulting in the development of tear-apart features. Here, we present a suite of concentric cylinder experiments aimed at studying the effects of cooling and shear rates on the rheology of a phonotephrite melt in response to crystallization. Experiments were conducted at: i) isothermal *subliquidus* temperatures of 1,167–1,189 °C and shear rates of 1–3 s^{-1}; ii) constant cooling rates of 1–10 °C/min and shear rates of 1–20 s^{-1}. We defined the viscosity-temperature-time window of lava solidification, as well as the transition from coherent flow to shear localization and physical separation (i.e., viscous rupture). Through this approach, we mapped the processes and timescales affecting pāhoehoe–ʻaʻā transition in natural lavas at variable cooling and shear rates. Under disequilibrium conditions, as the cooling rate increases, both crystallization onset and viscous rupture occur at lower temperature and earlier in time. Moreover, the time to reach the crystallization onset and viscous rupture also decreases with increasing shear rate. Both increasing cooling and shear rate reduces the critical crystallinity required for viscous rupture, a consequence of the non-linear interplay between temperature, crystallization kinetics, and melt viscosity. This outcome expands our knowledge on compositional, thermal, and rheological changes in phonotephritic systems. In addition to shear rate and apparent viscosity, comparison with previous measurements on basaltic systems indicates that the pāhoehoe–ʻaʻā transition is sensitive to the composition and cooling path of lavas.

Plain language summary

During flow on Earth's surface mafic lava flows frequently undergo a change in their surface morphology. They transition from smooth and continuous (pāhoehoe) to rough and fragmental (ʻaʻā) lava. This morphological transition is a result of changes in the lava's deformation style (i.e., rheology) as a response to flow. It affects both lava flow geometry and the efficiency of heat loss – ultimately governing lava advance rates and distances. Therefore, our ability to model and forecast lava emplacement and related hazards relies on the knowledge of the lava's syn-eruptive rheological evolution. We present an experimental study on the effect of deformation and cooling rates on the crystallization dynamics and rheology of a melt from Mt. Vesuvius (Italy). Combination of different experimental approaches (i.e., isothermal and cooling deformation experiments), enables measurements of the rheological evolution of the melt during crystallization. The resulting data track the transition in deformation style from coherent flow (pāhoehoe lavas) to surface rupture (ʻaʻā lavas) and provide the first systematic map of the pāhoehoe – ʻaʻā transition under variable cooling and deformation regimes. The presented results have important implications for the understanding and modeling of lava flow hazards and support strategies to mitigate volcanic risks.

1 Introduction

One of the main challenges in volcanology and petrology is to define and quantify the interdependence and timescales of processes acting during magma ascent through the crust as well as during eruption and emplacement of lava on the surface (Dingwell, 1996; Papale, 1999;

Gonnermann and Manga, 2007; Kolzenburg et al., 2017; Harris et al., 2020). Crystal nucleation and growth fundamentally control the multiphase rheology of lava and magma and, therewith, its transport efficiency (Pinkerton and Norton, 1995; Cashman et al., 1999; Hoover et al., 2001; Kilburn, 2004; Sato, 2005; Vona et al., 2011; Lanzafame et al., 2013; Kolzenburg et al., 2017, 2018a, 2020; Arzilli et al., 2019; Harris et al., 2020). Especially for mafic melts with low viscosities (η) and, therefore, fast kinetics due to rapid chemical diffusion, crystallization is widely recognized as a central mechanism governing magma transport and eruption style (Cashman et al., 1999; Cashman and Blundy, 2000; Sable et al., 2006; Gonnermann, 2015; La Spina et al., 2015, 2016; Moitra et al., 2018; Arzilli et al., 2019). Moreover, syn-emplacement crystallization is one of the key factors controlling the emplacement style and surface morphology during effusive eruptions (i.e., pāhoehoe – ʻaʻā transition; Emerson, 1926; Harris and Rowland, 2001; Hon et al., 2003; Kilburn, 2004; Soule and Cashman, 2005; Harris et al., 2020).

The implications for lava emplacement characteristics (e.g., wide and engulfing pāhoehoe sheet flows vs. self-channelized, bulldozing ʻaʻā flows) and the resulting hazards have been recognized for decades (Peterson and Tilling, 1980; Dragoni and Tallarico, 1994; Harris and Rowland, 2001; Giordano et al., 2007; Chevrel et al., 2013, 2018, 2019; Cordonnier et al., 2016; Kolzenburg et al., 2016, 2017, 2018a, 2020; Calabrò et al., 2020; Harris et al., 2020). The surface morphology of the lava also modulates heat loss from the flow and, with that, determines how far a lava may advance prior to solidification (Ramsey et al., 2019). Yet, the pāhoehoe – ʻaʻā transition has long been treated as a merely descriptive criterion of the surface morphology of lava flows, i.e., from a coherent and continuous flat or cleaved flow (pāhoehoe) to wrinkled detached masses of irregular shape (autobreccia) (Dutton, 1884; Emerson, 1926, Kilburn, 1990;

Harris et al., 2017). The onset of the pāhoehoe – ʻaʻā transition is characterized by the rupture of the lava's crust and the development of tear-apart structures, forming centimeter-scale protrusions known as cauliflower ʻaʻā (Kilburn, 1990; Harris et al., 2017). Little was known about the physical properties governing this transition until the study of Peterson and Tilling (1980), wherein the pāhoehoe – ʻaʻā transition assumed a physical connotation as the inverse relationship between the effective viscosity of the lava flow and the acting deformation rates. Temporal variations in lava viscosity was not taken into account and the transition was mainly ascribed to changes in shear rate related to the topography of the emplacement surface (e.g., Hon et al., 2003). However, a lava flow, at least in its exterior part, is commonly subject to thermodynamic disequilibrium conditions (continuous change of temperature, pressure and/or composition), where the effective viscosity can change as readily as the morphology of the emplacement surface (e.g., Huppert et al., 1984; Vetere et al., 2015; Giuliani et al., 2020). Unfortunately, our understanding of such non-linear processes is, to date, very limited. Seeing as the pāhoehoe – ʻaʻā transition represents a change in the rheological response of the suspension from pure viscous to more complex rheological behavior, it is critical to understand the competing mechanisms and timescales.

Currently, our knowledge of this rheological transition is restricted to basaltic systems and in particular to i) direct observations and measurements on active lava flows (e.g., Hon et al., 2003), ii) investigations on non-active lava flow (e.g., Peterson and Tilling, 1980; Duraiswami et al., 2014; Robert et al. 2014), and iii) a limited number of experimental studies on analog and natural materials (e.g., Cashman et al., 1999; Soule and Cashman., 2005; Sehlke et al., 2014; Soldati et al., 2017). These studies report a non-Newtonian behavior, defined by the onset of non-laminar deformation and increasing amounts of strain localization, with increasing crystal

content and shear rate. These experiments were conducted at isothermal conditions and stable suspension configurations (e.g., crystal content). As a result, the role of disequilibrium kinetics, typical of natural emplacement scenarios, has been so far overlooked.

In addition, the majority of experimental studies on natural magmatic compositions have investigated crystallization processes in the absence of deformation, under either equilibrium or disequilibrium conditions (e.g., Iezzi et al., 2014; Mollo and Masotta, 2014; Mollo and Hammer, 2017). Only a few studies (e.g., Kouchi et al., 1986; Vona and Romano, 2013; Chevrel et al., 2015; Kolzenburg et al., 2018a, 2020; Tripoli et al., 2019) have considered the interplay between deformation and crystallization kinetics from a rheological point of view. Their results highlighted the effect of melt advection in promoting crystallization and governing the rheological response of lavas and magmas.

Taking into account the state of knowledge and with the aim to mimic the solidification of low-viscosity (η) melts, we designed a set of experiments enabling us to systematically study the solidification process under both variable shear rate ($\dot{\gamma}$), cooling rate ($q = \Delta T/t$) and undercooling (ΔT). We focused on a phonotephrite melt from Vesuvius crystallizing leucite and clinopyroxene crystals. The final goal is to obtain a systematic mapping of pāhoehoe – ʻaʻā transition under variable cooling and deformation regimes leading to disequilibrium crystallization. The role of magma bulk composition in determining the rheological transition has been evaluated by comparing the present results with previous data on basaltic melts.

2 Crystallization experiments under deformation: state of the art

Rheological measurements conducted on high-T, low-η melts cooled from $T_{superliquidus}$ to $T_{subliquidus}$ (all symbols adopted in this study are listed in Table 1), are commonly performed with a concentric cylinder apparatus (Dingwell, 1986).

In recent years, Isothermal Deformation Experiments (IDEs) and Cooling Deformation Experiments (CDEs) were adopted to investigate the rheological evolution of natural magmatic compositions. IDEs are performed by imposing a certain shear rate ($\dot{\gamma}$) and initial cooling rate (q) from a *superliquidus* temperature to the final *subliquidus* target temperature (Fig. 1a). In these experiments it is assumed that the melt approaches a constant crystal volume fraction when a constant value of apparent viscosity (η_a) is reached in response to a specific initial undercooling (ΔT) and shear rate ($\dot{\gamma}$) (e.g., Vona and Romano, 2013). One advantage of IDEs is that the effects of crystal fraction and shape, as well as changes in the residual melt composition on the measured η_a, can be constrained by post-experiment sampling and further textural analysis (e.g., Sato, 2005; Ishibashi and Sato, 2007; Ishibashi, 2009; Vona et al., 2011; Vetere et al., 2013a; 2017; 2020; Sehlke et al., 2014; Chevrel et al., 2015; Campagnola et al., 2016; Soldati et al., 2016, 2017; Morrison et al., 2020; Sehlke and Whittington, 2020). Empirical and/or theoretical models of multiphase suspensions, commonly derived from experiments on synthetic or analog materials can be tested and improved via this method (see Mader et al., 2013 for a review).

On the other hand, CDEs are carried out to capture the transient rheology of magmas and lavas under variable $\dot{\gamma}$ and q relevant to natural emplacement conditions (Fig. 1b; Giordano et al., 2007, Kolzenburg et al., 2016, 2017, 2018a, b; 2019, 2020; Vetere et al., 2019, 2020). CDEs allow to better approximate the natural thermal history of lavas and magmas related to transport and emplacement, such as for lavas flowing on Earth's surface (Giordano et al., 2007; Kolzenburg et al., 2017, 2018 a, b), and to quantify the cut-off temperature (i.e., the threshold at

which the lava flow becomes immobile from a rheological point of view; Kolzenburg et al., 2016, 2017, 2018 a, b, 2020). However, CDEs do not lend themselves to post experimental quantification of composition or textural features (i.e., crystal contents and distribution), because rapid quench is technically challenging (e.g., Kolzenburg et al., 2018 a, b).

Both IDEs and CDEs document the effect of deformation on crystallization kinetics and, therefore, the rheological evolution of lava and magma at $T_{subliquidus}$. An increasing deformation rate promotes nucleation and growth of crystals by i) lowering the time lag of nucleation by increasing the random collision between atoms (incubation time, t_{inc}; Kouchi et al., 1986; Vona and Romano, 2013; Kolzenburg et al., 2018a) and ii) supplying fresh melt to the growing crystal surface (Vona and Romano, 2013; Kolzenburg et al., 2016, 2018b). Under both constant cooling and constant undercooling conditions, t_{inc} progressively decreases with increasing cooling rate (i.e., nucleation delay; Hammer, 2006, 2008; Iezzi et al., 2008; Mollo et al., 2012, 2013; Kolzenburg et al., 2016; Rusiecka et al., 2020; Vetere et al., 2020), until reaching a critical cooling rate (q_c) at which crystallization is suppressed (Vetere et al., 2015 and references therein), thereby leading to glass formation.

In this study, we combined IDEs and CDEs to delineate the viscosity-temperature-time (η-T-t) conditions relevant to the crystallization of phonotephrite melts. Within the identified η-T-t window, we mapped the effects of $\dot{\gamma}$, ΔT and q on the crystallization kinetics and, consequently, on the rheological evolution of the melt under disequilibrium conditions. These measurements tracked the effective viscosity of the suspension until the sharp transition from flowing as a coherent unit (i.e., laminar deformation) to tearing apart along surfaces sub-parallel to the direction of maximum shear (rotational axis of the concentric cylinder spindle), representing a threshold limit in the effective shear stress that the melt is able to sustain without losing

coherence during flow (i.e., "rupturing", according to Kilburn, 1990 and Harris et al., 2017). This rupture process is recorded in the experiments by a significant drop in the measured shear stress, thus defining the pāhoehoe – ʻaʻā transition.

3 Experimental strategy

3.1 Starting material and sample preparation

The starting material used in this study is a leucite-bearing phonotephrite from 472 CE Pollena subplinian eruption of Somma-Vesuvius volcano (NA bed; Sulpizio et al., 2005; Vona et al., 2020). Despite its explosive origin, the chemistry of the selected sample is also representative of the composition of the more evolved lavas erupted during the post-1631 CE activity at Vesuvius (Fig. S1; Belkin et al., 1993). The powdered natural juvenile material (lapilli-sized scoriae) was melted in a thin-walled Pt-crucible using a Nabertherm $MoSi_2$ chamber furnace. Melting was carried out at 1,400 °C and air oxygen fugacity by maintaining the temperature constant over 5 h and then quenching the melt to a glass in air. To ensure chemical homogeneity and complete removal of bubbles from the melt, glass chips from different melting batches were re-melted into the experimental $Pt_{80}Rh_{20}$ crucible (62, 32, and 1.5 mm in height, inner diameter, and wall thickness, respectively) and stirred at 10 s^{-1} with a $Pt_{80}Rh_{20}$ spindle (3.2 and 42 mm in diameter and length, respectively) in air at 1,400 °C for 6 hours. Chemical homogeneity was verified by constant viscosity readings among the different melting batches. The experiments were performed in a Rheotronic II Rotational Viscometer (Theta Instruments) at the EVPLab of the University of Roma Tre. The apparatus is equipped with an Anton Paar Rheolab Qc viscometer head (full-scale of torque of 75 mNm). The system was calibrated against the NIST

717a standard reference material providing an accuracy better than 0.06 log units. Temperature measurements were performed with a S-type thermocouple with accuracy of ±2 °C. At the end of each experiment, the sample was quenched at ~120 °C/min by holding the crucible walls under flowing water (Campagnola et al., 2016). Microscope examination and Raman spectroscopy ruled out the presence of microlite and nanolite crystals in the synthesized glass (Di Genova et al., 2017).

The chemical composition of the starting glass is reported in Table S1. Microchemical analysis was carried out using a Jeol-JXA8200 electron microprobe equipped with five wavelength dispersive spectrometers at the HP-HT Laboratory of Experimental Volcanology and Geophysics (HP-HT Lab) of the Istituto Nazionale di Geofisica e Vulcanologia in Roma (Italy). A detailed description of the analytical conditions and standards is reported in Iezzi et al. (2008). Briefly, a slightly defocused 3 μm beam was used with a counting time of 5 s on background and 15 s on peak. The following standards were used for calibration: jadeite (Si and Na), corundum (Al), forsterite (Mg), andradite (Fe), rutile (Ti), orthoclase (K), barite (Ba), apatite (P), spessartine (Mn) and chromite (Cr). Sodium and potassium were analyzed first to prevent alkali migration effects. Based on counting statistics, accuracy was better than 1–5% except for elements with abundances below 1 wt.%, for which accuracy was better than 5–10%. Precision was typically better than 1–5% for all analyzed elements.

3.2 Crystal-free melt viscosity

The high-T viscosity of the anhydrous melt (η_{liquid}) was measured using the concentric cylinder set-up described above. Viscosity was calculated from the shear stress and shear rate distributions, based on the cylindric geometry of the crucible and spindle (Stein and Spera,

1998). Measurements were performed between 1,450 and 1,199 °C in steps of 50 °C, at ambient pressure, air oxygen fugacity, and constant shear rate of 5 s^{-1}. The temperature was maintained constant at each step until a stable value of η_{liquid} was achieved (typically 45 minutes). The pure η_{liquid} was also measured between 680 and 760 °C by micropenetration technique using a Setaram SETSYS Evolution TMA vertical push-rod dilatometer (e.g., Di Genova et al., 2014). These low-*T* measurements were performed under Argon atmosphere at 1 bar on doubly polished glass disks with diameter and thickness of 10 and 3 mm, respectively, and an indentation force of 0.98 N. The apparatus was calibrated against the standard glass DGG-1 (Meerlender, 1974). Results from both high- and low-*T* measurements are reported in Table S2.

3.3 Methodology used for IDEs and CDEs

IDEs and CDEs were carried out using the same concentric cylinder apparatus and geometry adopted for η_{liquid} measurements. Pre-experiment melt homogenization and thermal equilibration (i.e., *superliquidus* treatment) was performed by stirring the melt at 1,400 °C, ambient pressure, and air oxygen fugacity for ~1 h at $\dot{\gamma}$ of 10 s^{-1}.

Three IDEs were conducted at 1,189 (PoX15), 1,178 (PoX17), and 1,168 (PoX18) °C by employing a shear rate of 1 s^{-1}. Conversely, one IDE (PoX19) was performed at 1,167 °C and a shear rate of 3 s^{-1}. All the experiments were cooled from 1,400 °C to the target temperature at a rate of 12.5 °C/min. The viscosity-time evolution followed the trend described in Fig. 1a, up to the achievement of a time-independent η_a that is indicative of a stable crystal content (e.g., Vona and Romano, 2013). At this stage, the shear rate dependence of the suspension viscosity was investigated by varying systematically the shear rate between 3 and 0.1 s^{-1} (see Fig. S3 in Supporting Information and cf. Campagnola et al., 2016).

For CDEs, two different experimental subsets were designed at variable cooling rate and constant shear rate (i.e., CDE-q set) and, *vice versa*, at variable shear rate and constant cooling rate (i.e., CDE-$\dot{\gamma}$ set). The CDE-*q* set was carried out at constant shear rate of 5 s^{-1} and variable cooling rates of 1, 3 5, and 10 °C/min. The CDE-$\dot{\gamma}$ set was carried out at constant cooling rate of 1 °C/min and variable shear rates of 1, 2.5, 5, 10, and 20 s^{-1}. At the end of each cooling segment, the sample was re-heated to 1,400 °C and re-homogenized for 1 h at a shear rate of 10 s^{-1}, before starting the next experiment. The recovery of a viscosity reading within 1% of previous measurements at T = 1,400 °C was taken as evidence for complete re-melting of crystalline phases formed in previous experiments. In a few cases, at the end of the experiment, the sample was extracted and quenched for visual inspection of the surface morphology. Overall, the applied cooling and shear rates mimic conditions relevant to lava flow emplacement (Giordano et al., 2007; Chevrel et al., 2013, 2019; Cordonnier et al., 2016; Kolzenburg et al., 2017, 2018a, 2019, 2020; Harris et al., 2020).

All experiments were terminated either upon reaching the torque limit of the device (i.e., 75 mNm) or upon reaching a stress-drop indicative of non-Newtonian behavior (Fig. 1b). Note that the melt viscosity and shear rates imposed here result in flow conditions that are significantly lower than those required for fragmentation of the magma (Arzilli et al., 2019) and the onset of unrelaxed behavior of the melt phase (Webb and Dingwell, 1990). Melt relaxation times ($t_r = \eta_0/G_\infty$, where $G_\infty = 10^{10\pm0.5}$ Pa; Whittington et al., 2012) at our experimental conditions span between 10^{-7} and 10^{-6} s. Therefore, no magma fragmentation or viscoelastic deformation and brittle fracture of the melt phase occurred (Dingwell, 1996); all processes remain in the viscous regime (e.g., Jones et al., 2019) and the observed behavior can be described as "viscous rupture" (i.e., the transition of coherent flow to shear localization physical

separation; see Section 4.2.2.3). At the end of each IDE and CDE cycle, the spindle was removed and the sample was quenched at 120 °C/min by holding the crucible walls under a water flow. For IDEs, the post-experiment sample was drilled, sectioned both in transverse and longitudinal sections, and polished for textural and chemical analyses. The chemical compositions of the residual glasses (Table S1) were measured at the HP-HT Lab of the INGV, as described above. Textural analysis of IDEs was performed by optical and scanning electron microscopy (SEM). Optical microscopy was used to map each sample as a mosaic of ~200 images at 10× magnification (image resolution of 286 pixels/mm). Back-scattered electron (BSE) photomicrographs were acquired using a Philips XL30 installed at the Interdepartmental Electron Microscopy Laboratory (LIME) of the University of Roma Tre at 120× magnification (1747 pixels/mm). Photomicrographs were processed using ImageJ software (imagej.nih.gov/ij/). Crystal fractions were obtained by integrating the crystal content measured at different magnifications using custom built Matlab© codes (see Vona et al., 2017 for a detailed methodology). Mean crystal shapes (expressed by the mean aspect ratio of particles, R) were estimated using CSDslice5 software (Morgan and Jerram, 2006).

3.4 Net effect of crystals on viscosity

For each experiment, the relative viscosity (η_r) expressed as the ratio of the apparent viscosity of the suspension (η_a) and the viscosity of the residual melt (η_0), was calculated in order to evaluate the crystallization-induced rheological departure from the pure melt behavior.

For IDEs, η_r was estimated using the GRD model (Giordano et al., 2008) and the residual glass composition (Table S1). For CDEs, in order to overcome the inability of analyzing the residual melt chemistry, η_r has been estimated by normalizing η_a to the value of η_{liquid} predicted

by the VFT model (Tamman and Hesse, 1926), obtained by fitting the viscosity data of the pure melt, as illustrated in Kolzenburg et al. (2017) (see also Section 4.1). It should be noted that the VFT equation estimates the *T*-dependent viscosity of the initial phonotephritic melt. This approximation does not take into account the effect of crystallization-induced melt compositional change to the suspending melt viscosity (i.e., $\eta_0 \neq \eta_{liquid}$). This effect is estimated to be within 0.1 log Pa s, as evidenced by the comparison with GRD viscosity modeling (Giordano et al., 2008) of IDEs, for which chemical compositions of the residual glasses are available (Table S1, Fig. S2 in Supporting Information). The effect of crystallization on melt composition is also in reasonable agreement with previous estimates conducted on basaltic melts (0.06-0.18 log Pa s from Vona et al., 2011; 0.20-0.61 log Pa s from Sehlke et al., 2014; 0-0.05 log Pa s from Soldati et al., 2016; 0-0.55 log Pa s from Soldati et al., 2017; 0.03 log Pa s from Kolzenburg et al., 2017).

The relative viscosity values determined by this approach are used in the following sections to identify the onset of crystallization for the constant cooling experiments and to estimate crystal fractions using suspension rheology models (Vona et al., 2011). We define the crystallization onset at the temperature and time (T_{dep} and t_{dep}, respectively) at which a rise of 0.05 log units followed by a continuous increase in η_r is observed.

4 Results

4.1. Crystal-free melt viscosity

Values of η_{liquid} obtained from high- and low-*T* measurements are in the ranges of $10^{1.14}$-$10^{2.38}$ Pa s (1,450-1,199 °C) and $10^{9.04}$-$10^{11.98}$ Pa s (760-680 °C), respectively. The results (Fig.

S2; Table S3) describe a non-Arrhenian temperature-dependence of viscosity that can be modeled using the VFT equation (Tammann and Hesse, 1926) as: log η_{liquid} = -2.945 + [4280 / (T – 668.6)]. Measurements of η_{liquid} are reproduced with a Root Mean Square Error (RMSE) of ±0.04 log Pa s, and are also consistent with predictions from GRD model with RMSE of ±0.16 log Pa s (Table S2).

4.2. Rheology of the crystal-bearing melt

4.2.1 IDE results

The temporal evolution of apparent viscosities is shown in Fig. 2a. All measurements follow the schematic path displayed in Fig 1a. *Superliquidus* viscosity values at 1,400 °C and before detectable crystallization (at 1,189, 1,178, 1,168, and 1,167 °C) agree with melt data modeled by VFT equation. According to the viscosity increase resulting from crystallization, the values measured at the steady state conditions range between 2.69 and 3.62 log Pa s (Table 2).

As initial ΔT increases with decreasing $T_{subliquidus}$, the length of the viscosity plateau before the onset of crystallization decreases, responding to a decreasing incubation time (Kouchi et al., 1986). On the other hand, PoX18 and PoX19 were carried out at similar $T_{subliquidus}$ but different $\dot{\gamma}$ of 1 and 3 s^{-1}, respectively. Comparison shows that the final viscosity value increases significantly from 3.07 to 3.62 log Pa s with increasing $\dot{\gamma}$. At the steady state condition, crystal-bearing melts undergo a shear-thinning effect on the order of ~0.10-0.15 log Pa s (Table 2, Fig. 2a inset and Fig. S3).

Textural analysis shows that the mineral assemblage consists of leucite and clinopyroxene (Fig. 3). The crystal content (ϕ) increases from 0.09 to 0.29 as a function of initial ΔT and deformation rate (Table 2), paralleling the same trend of viscosity data (Fig. 2a). Leucite crystals

are large and commonly skeletal, whilst clinopyroxene crystals show prismatic and slightly elongated shapes (Fig. 3). Glomerocrysts and leucite-clinopyroxene intergrowths are systematically more abundant with increasing initial ΔT and $\dot{\gamma}$ (Fig. 3). The residual glass is characterized by minor compositional changes (Table S1), with a slight increase in SiO_2 and Na_2O with increasing crystal volume fraction. This compositional variability causes a weak increase (0.01-0.18 log Pa s) of η_0 (calculated by the GRD model; Table 2) with respect to the viscosity of the starting material composition (η_{liquid}).

The value of η_r is plotted in Fig. 2b as a function of ϕ. The crystallinity has minor effects on the relative viscosity at $\phi < 0.15$ (i.e., PoX15, PoX17, and PoX18). As a consequence, the apparent viscosity η_a is only slightly higher than that of the suspending liquid (η_0), with η_r ranging from 1.2 to 1.6. Conversely, at ϕ of 0.29 (i.e., PoX19), the effect of crystallinity is more pronounced, resulting in η_r between 6 and 8, as a function of $\dot{\gamma}$. The value of η_r is in good agreement with that predicted by the model of Vona et al. (2011) for crystal-bearing suspension viscosity. At lower crystal contents ($\phi < 0.15$), the model trend matches with values of η_r at R close to 1 (Fig. 2b), whereas at higher crystal contents ($\phi \geq 0.29$), data are better reproduced for R of 3-4 (Fig. 2b), in agreement with mean R values obtained by textural analysis (Tab. 2).

4.2.2 CDE results

4.2.2.1 CDE-*q*

Results for CDE-*q* (constant $\dot{\gamma}$ of 5 s^{-1}) are presented in Figure 4a, b, c. Fig. 4a shows that the rheological evolution of CDE-*q* at *superliquidus* condition follows the VFT model of the crystal-free melt, depicting a smooth increase of viscosity with decreasing temperature. This trend continues to *subliquidus* condition (Fig. 4a), until the viscosity-temperature curve departs

from η_{liquid} at the onset of crystallization (i.e., T_{dep}, Fig. 1b). The rheological T_{dep} decreases from 1,130 to 1,070 °C, as q increases from 1 to 5 °C/min (Fig. 4a; Table 3) for all experiments, with exception of the experiment at q of 10 °C/min where no crystallization is observed. Additionally, as q increases from 1 to 5 °C/min, the time at which the crystallization takes place decreases from 270 to 66 min (Fig. S4a; Table 3). At the rheological departure, η_{liquid} increases from 2.90 to 3.34 log Pa s with increasing q (Fig. 4a; Table 3). At the onset of crystallization, the magnitude of crystal growth kinetics scales with the increase of relative viscosity (η_r) and, therefore, can be evaluated as a function of temperature ($d\eta_r/dT$) and time ($d\eta_r/dt$). Note that the viscosity increase during crystallization ($T < T_{onset}$) is not smooth but, rather, it is marked by small precursor stress drops. We report the slopes of the curves averaged over the range between T_{onset} and the final stress drop. The average value of $d\eta_r/dT$, represented by the mean slope of the curves over the range between T_{onset} and the final stress drop in Fig. 4c, decreases by a factor of 5 from 0.039 to 0.007 log units $°C^{-1}$ with increasing q. The variability of $d\eta_r/dt$ reduces to 0.036-0.076 log min^{-1} (factor of 2, Fig. S4a). All measurements reach a threshold value where the shear stress drops rapidly due to the transition from a pure viscous response to viscous rupture (Fig. 4a, b, c). At a constant shear rate of 5 s^{-1}, the temperature at which this stress drop occurs decreases from 1,106 to 1,003 °C, as the q increases from 1 to 5 °C/min (Fig. 4 a, b, c). The time to reach the stress drop also decreases from 294 to 79 min as q increases from 1 to 5 °C/min (Fig. S4; Table 3). However, the shear stress at the stress drop increases from ~ 4.7 to ~ 5.3 log Pa (Fig. 4b), translating to an apparent viscosity of ~ 4.0 to ~ 4.6 log Pa s (Fig. 4a; Table 3). At the same time, η_r decreases from 0.94 to 0.47 (Fig. 4c), as q increases from 1 to 5 °C/min (Table 3). No departure from the VFT model is observed at q of 10 °C/min (stopped at T of 972 °C), owing to minor or absent crystallization and, hence, negligible effects on the apparent viscosity (Fig. 4a).

4.2.2.2 CDE-$\dot{\gamma}$

Results for CDE-$\dot{\gamma}$ (constant q of 1 °C/min) are presented in Figure 4d, e, f. Fig. 4d shows that the rheological evolution of CDE-$\dot{\gamma}$ follows that observed for η_{liquid} at high temperatures. The onset of crystallization is marked by a departure from the VFT curve occurring at T increasing from 1,110 to 1,146 °C and t decreasing from 290 to 254 min with increasing $\dot{\gamma}$ (from 1 to 20 s^{-1}; Fig. 4d, S4 and Table 3). The corresponding melt viscosity at the onset of crystallization decreases from 3.06 to 2.77 log Pa s (Table 3). The kinetics of crystal growth in CDE-$\dot{\gamma}$ explore a narrow $d\eta_r/dT$ range of 0.038-0.055 log units $°C^{-1}$ (i.e., see the sub-parallel trends displayed in Fig. 4f), corresponding to $d\eta_r/dt$ range of 0.038-0.055 log units min^{-1}. At $\dot{\gamma}$ of 1 s^{-1}, the viscosity increases continuously in response to cooling and crystallization and the experiment was terminated at T = 1,080 °C upon reaching the torque limit of the rheometer, corresponding to η_a of ~5 log Pa s at the imposed $\dot{\gamma}$ of 1 s^{-1}. In all the experiments, small and intermitted stress drops were observed, as for the case of CDE-q (Fig. 4d, e, f). Main stress drops took place at higher T (from 1,100 to 1,134 °C, Fig. 4e) and shorter t (from 300 to 266 min, Fig. S4 and Table 3) as $\dot{\gamma}$ increases from 2.5 to 20 s^{-1}. The absolute value of viscosity at the stress drop decreases from 4.4 to 3.5 log Pa s with increasing $\dot{\gamma}$ (Table 3). The peak stress values fall within a narrow range of ~ 4.7-4.8 log Pa for all the experiments (Fig. 4e). In terms of log η_r, peak values ranged from 0.66 to 1.27 with decreasing $\dot{\gamma}$ (Fig. 4f). The maximum value of log η_r ~ 1.6 (Fig. 4f) is reached in the experiment carried out at $\dot{\gamma}$ of 1 s^{-1} at which no stress drop was observed.

4.2.2.3 Surface morphology of post-experimental samples

The relatively slow quench rate dictated by the concentric cylinder set-up, combined with the fast crystallization kinetics of CDEs, prevents meaningful quantitative textural and chemical analyses of post-experimental samples (Kolzenburg et al., 2018a, b). Nonetheless, visual inspection of the surface morphology of representative samples (Fig. 5) can provide valuable, qualitative textural information on the complex rheology and surface features of the melt in response to cooling and crystallization (see Sehlke et al, 2014). For example, the sample collected after measuring η_{liquid} (Fig. 5b) shows a smooth glassy surface, with well-defined spiral-shaped flow lines. Conversely, at the end of the controlled cooling path (Fig. 5c), the melt surface having undergone viscous rupture is more jagged with evident heterogeneities due to development of tear-apart structures and protrusions akin to those observed on cauliflower lavas (see discussion below). Once completely solidified (Fig. 5d), the sample surface preserves these complex morphologies that are accompanied by abundant crystallization of leucite agglomerates (light green in Fig. 5d).

5 Discussion

5.1 Thermo-rheological diagram of the phonotephrite melt

By integrating and interpolating data from IDEs and CDEs, we can derive a rheological map that quantifies the effects of ΔT, q, and $\dot{\gamma}$ on the crystallization kinetics and the changes in the rheological properties of leucite-bearing phonotephrites at ambient pressure and air oxygen fugacity (Fig. 6). This approach allows to define the viscosity-temperature-time (η-T-t) window of the entire crystallization process up to steady crystal content (i.e., IDE) or the achievement of viscous rupture for cooling rates equal to or higher than 1 °C/min (i.e., CDE). The field in which

disequilibrium kinetics govern the rheological evolution of magmas and lavas is bound by two distinct limits in viscosity-temperature space: 1) the maximum viscosity limit of the suspension, which is defined by the equilibrium crystal fraction at any *subliquidus* temperature for $t > t_{eq}$ (where t_{eq} is the time to achieve a thermodynamic equilibrium) and 2) the minimum viscosity limit of the system, defined by the crystal-free melt viscosity before the onset of crystallization at $t < t_{inc}$ or in response to fast cooling rates favoring glass formation at $q > q_c$. These two boundaries constrain the η-T-t window relevant for disequilibrium transport of a given suspension in which the crystallization kinetics (sensitive to the effects of q and $\dot{\gamma}$) and the resulting rheological responses can be mapped, also including the transition from continuous flow to viscous rupture.

Results from IDEs indicate that a steady viscosity value between ~2.7 and 3.6 log Pa s is achieved after ~ 11-20 hours, depending on initial ΔT (Fig. 2a). The final viscosity plateau is indicative of a stable crystal content ϕ (Fig. 1a) ranging between 0.09 and 0.29 (Fig. 2b and 3). In order to test the achievement of thermodynamic equilibrium and to constrain the upper viscosity boundary (Fig. 6), we performed several numerical simulations of equilibrium crystallization using the MELTS code (Ghiorso and Sack, 1995; Asimow and Ghiorso, 1998). We simulated IDEs by equilibrating the phonotephrite bulk composition at 1 atm, air redox conditions, and melt-H_2O contents between 0.01 and 0.1 wt.% (i.e., nominally anhydrous atmospheric pressure experiments according to Behrens and Gaillard, 2006). Starting from $T_{liquidus}$ of 1,273 °C, modeling results track the melt crystallization up to ϕ of ~ 0.40 at T of 1,080 °C. These crystal contents were converted into apparent viscosity using i) the residual melt viscosity estimated via the GRD viscosity model (Giordano et al., 2008) and ii) the two-phase viscosity model of Vona et al. (2011) (R of 1-4) to account for the mechanical effect of suspended crystals on η_a. The

computed viscosities are in good agreement with values measured during IDEs (Fig. 6), suggesting that near-equilibrium crystallization conditions were achieved. Combined, these data define the upper viscosity boundary of the thermo-rheological regime-diagram for the phonotephritic melt. As observed by Kouchi et al. (1986), melt deformation enhances crystal nucleation and growth processes, resulting in shorter incubation times and higher crystal growth rates at constant undercooling and cooling rates. This, in turn, promotes faster achievement of equilibrium crystal contents (Vona and Romano, 2013). Within the IDEs, PoX18 and PoX19 experiments conducted at variable shear rates (1 and 3 s^{-1}, respectively) and nearly identical T (1167-1168 °C), show different incubation times (180 and 120 min, respectively), plateau viscosity values (~3.1 and 3.6 log Pa s, respectively), and crystal contents (0.14 and 0.29, respectively). The measured crystal fractions bracket the value predicted by the thermodynamic modeling (ϕ of ~ 0.20). Moreover, as observed by previous studies (Kouchi et al., 1986; Vona and Romano, 2013), the nucleation density increases with increasing shear rate, leading to the formation of smaller leucite and clinopyroxene crystals in PoX19 (Fig. 3). At the same time, in PoX19 the higher amount of elongated clinopyroxene crystals affects the mean R value (R of 3-4 in PoX19 compared to R of 1 in PoX18) yielding to a more pronounced effect on the apparent viscosity (Fig. 2a, b, 6; Mader et al., 2013).

The low-η boundary of *subliquidus* melt viscosity is defined by the curve of crystal-free liquid (Fig. 6). Once the melt is rapidly cooled, the crystallization is suppressed and *subliquidus* melt viscosity depends solely on the η_{liquid}-T dependence described by VFT fit (Fig. S2). In CDE-q, the onset of crystallization is rheologically detected at q < 5 °C/min. Conversely, at q of 10 °C/min, the crystallization is suppressed to the point of not affecting the measured viscosity (Fig. 4a). This documents that, in the investigated T range, the glass forming ability of phonotephritic

composition is bound by a critical cooling rate (q_c) between 5 and 10 °C/min. Similar q_c values (≥ 5 °C/min) were observed by Giordano et al. (2007) and Vetere et al. (2020) in constant shear and cooling rates experiments carried out on foiditic (Mount Nyiragongo volcano, Democratic Republic of Congo) and shoshonitic (Vulcanello, Aeolian Archipelago, Italy) compositions, respectively.

5.2 Effect of q and $\dot{\gamma}$ on disequilibrium crystallization kinetics

The viscosity evolution measured by CDE-q and CDE-$\dot{\gamma}$ experiments (Fig. 4) allows to discriminate two main parameters important for the crystallization kinetics of solidifying magmas and lavas: i) the incubation time to the onset of crystallization from $T_{liquidus}$ to T_{dep} and ii) the effective crystallization rate corresponding to the change in relative viscosity slope at $T < T_{dep}$ ($d\eta_r/dT$; Fig. 4c, f) . This represents a major advantage with respect to standard (i.e., unstirred) crystallization experiments (e.g., Mollo and Hammer, 2017), where crystallization kinetics are not monitored in real time and can be only time-averaged from *liquidus* to quench T (unless experiments are coupled with calorimetry; see Giuliani et al., 2020). In the following, the two different stages (i.e. departure from crystal-free liquid and crystallization) are analyzed to deduce the effects of both q and $\dot{\gamma}$ on the disequilibrium crystallization of the phonotephrite melt.

5.2.1 Onset of crystallization

Data from this study indicate that q exerts a primary control on the rheological evolution of the crystallizing suspension (Fig. 4a, b and c). Departure from η_{liquid} occurs at progressively higher T with decreasing q. Since T_{dep} can be regarded as a proxy for the onset of crystallization (i.e., $T_{dep} \approx T_{onset}$; Kolzenburg et al., 2017), it is apparent that crystal saturation takes place at

progressively lower degrees of undercooling ($\Delta T_{onset} = T_{liquidus} - T_{onset}$) with decreasing q (e.g, Kolzenburg et al., 2017; 2020 and references therein).

The data can also be presented as a TTT diagram (e.g., Chevrel et al., 2015; Kolzenburg et al., 2021; Fig. 7). Fig. 7a shows that the magnitude of q also affects the timescale of crystallization. As q decreases from 5 to 1 °C/min, the onset of crystallization is recorded after longer experimental times. The observed behavior agrees with classic nucleation theory where ΔT_{onset} required to stabilize the crystal nuclei decreases with decreasing q, whereas the incubation time (t_{inc}) progressively increases due to nucleation delay (Hammer, 2006; Iezzi et al., 2008; Mollo et al., 2012, 2013; Kolzenburg et al., 2016; Giuliani et al., 2020; Rusiecka et al., 2020; Vetere et al., 2020).

From a rheological perspective, the crystallization takes place from a melt with progressively higher viscosity (lower T_{onset}) with increasing q, and *vice versa*. Moreover, crystallization starts significantly earlier in time at fast q. This is a result of the balance between crystallization kinetics and cooling rate. The faster increase of melt viscosity with increasing q reduces the diffusion of cations in the melt phase and, consequently, crystal nucleation and growth are hampered until reaching the critical cooling rate, where crystallization is kinetically suppressed with formation of a pure glass phase (Fig. 7a; Iezzi et al., 2008; Vetere et al., 2013b).

Results from CDE-$\dot{\gamma}$ also document that $\dot{\gamma}$ affects the time required to reach the onset of crystallization (Fig. 7b), although the magnitude of this effect is lower than that of q. As $\dot{\gamma}$ increases from 1 to 20 s^{-1}, the departure from a pure liquid behavior (onset of crystallization) takes place earlier in time and at higher T (Fig. 7b). This highlights the role of $\dot{\gamma}$ in facilitating crystallization due to a lower incubation time and echoes with the results from IDEs (Fig. 2a), as

well as data presented in previous works (Kouchi et al., 1986; Vona et al., 2011; Vona and Romano, 2013; Kolzenburg et al, 2017, 2018a).

5.2.2 Effective crystallization rate

Using the equation proposed by Vona et al. (2011), assuming *R* variable from 1 to 4, we have modeled the evolution of η_r through time in terms of crystal volume fraction. Following Kolzenburg et al. (2020), the temporal variation of crystallinity can be used to derive the average volumetric crystallization rate parameter. Computed rates range from 0.0095 to 0.0189 cm^3/s for CDE-q and from 0.0095 to 0.0151 cm^3/s for CDE-$\dot{\gamma}$ (Table 3). These values are comparable with those inferred for plagioclase in basaltic melts at similar q and $\dot{\gamma}$ conditions (see Kolzenburg et al., 2020). No systematic variation of volumetric crystallization rate has been observed as a function of either q or $\dot{\gamma}$. Moreover, their limited range of variability suggest that, while both q and $\dot{\gamma}$ deeply affect the crystallization onset (i.e. incubation times), their effect on the effective growth rate is subordinate and more difficult to discern. Note that Kolzenburg et al. (2020) report data on plagioclase crystallization, whereas the crystals growing from this melt are leucite and pyroxene. The striking similarity in the recovered crystallization kinetics implies that for cooling and shear rates expected at lava flow emplacement conditions, the environmental conditions are the core driver for the viscosity evolution while the nature of the phases appears to play only a secondary role that modulates the overall process. This suggests that different melt compositions may follow very similar paths of viscosity evolution during emplacement under disequilibrium conditions, and has far-reaching consequences for lava flow emplacement modeling.

5.3 Effects of q and $\dot{\gamma}$ on the rheological evolution of melt and viscous rupture

Fig. 4 shows that both q and $\dot{\gamma}$ affect the rheological evolution of the melt and constrain the *t-T* conditions for the transition from continuous viscous flow to viscous rupture (i.e., drop of viscosity in Fig 4a,d and drop in stress Fig. 4b,e). We define the transition at the point of maximum apparent viscosity or shear stress as η_{vr} and τ_{vr}, respectively (Fig. S5).

Previous experiments on analog (Soule and Cashman, 2005) and natural basaltic materials (Sehlke et al., 2014) indicate that the transition from pure viscous flow to viscous rupture can be defined as a transition field in shear rate and apparent viscosity space. This is in agreement with field observations on the pāhoehoe – ʻaʻā transition in natural lava flows (Peterson and Tilling, 1980; Cashman et al., 1999; Hon et al., 2003). In particular, Soule and Cashman (2005) describe that, when the crystal fraction exceeds the percolation threshold (cf. Saar et al., 2001; Saar and Manga, 2002), flow instabilities arise from particle-particle interactions. This leads to different degrees of shear localization, from particle clumping to shear zone formation and detachment. Soule and Cashman (2005) ascribe this phenomenon to an increasing solid fraction and/or shear rate, denoting that the formation and accretion of particle clusters increases with these two parameters. The final effect is the development of strain localization and, ultimately, the onset of viscous rupture.

The viscosity evolution displayed in Fig. 4 for CDE-q and CDE-$\dot{\gamma}$ experiments suggests that a rheological transition is achieved in response to higher amount of crystallization. In particular, η_a and η_r data highlight that, after the onset of crystallization, the viscosity increase is discontinuous and characterized by a series of small stress drops ($\Delta\eta < 0.1$ log Pa s) leading up to the final viscous rupture (Fig. 4 and Fig. S5). These stress drops are absent before the onset of crystallization and, on this basis, we speculate that they represent small ruptures potentially related to crystal-crystal interaction and shear localization. At low crystal volume fractions, the

higher volume of interstitial melt allows ruptures to rapidly heal, resulting in the recovery of the measured shear stress. On the other hand, with increasing crystal content and decreasing temperature, healing of such ruptures is less and less efficient, likely also due to the increasing amount and size of asperities on the rupture surface. Small ruptures may coalesce in response to shear strain and may ultimately lead to a major shear localization event (i.e., viscous rupture) producing the final, large, stress drop that follows η_{vr} peak. Such complex rheological behavior is preserved macroscopically and texturally in the solidified samples, showing a non-uniform surface morphology, made up of protrusions, tear-apart structures, and detachments (Fig. 5c, d).

The timescale (t_{vr}) to reach viscous rupture is dictated by the crystallization kinetics that, in turn, are controlled by cooling and shear rates. These two parameters determine the attainment of a critical mechanical state for the suspension that is described by the peak shear stress (τ_{vr}) observed at the point of viscous rupture. Viscous rupture is measured at $\dot{\gamma} > 1$ s^{-1} (Fig. 7b) during constant cooling at 1 °C/min (CDE-$\dot{\gamma}$) and occurs in a very narrow range of τ_{vr} between 4.7 and 4.8 log Pa (Fig. 4e). Data suggest an almost constant rupture strength of the suspension, which is lower than the rupture strength assumed for crystal-free silicate melts (10^8, Pa, Dingwell, 1996; Cordonnier et al., 2012). At the same time, the suspension viscosity at the viscous rupture (η_{vr}) decreases from ~ 4.4 to ~ 3.5 log Pa s as $\dot{\gamma}$ increases from 2.5 to 20 s^{-1} (Fig. 4d). At constant $\dot{\gamma}$ of 5 s^{-1} (CDE-q), τ_{vr} increases from 4.7 to 5.3 log Pa (~ 0.6 log units), as q increases from 1 to 5 °C/min (Fig. 4b). The difference in the rupture strength may be explained by the variable timescales and temperature regimes of the experiments that influence the crystallization kinetics in terms of development of a crystal framework and magnitude of the suspending melt viscosity.

With increasing $\dot{\gamma}$, viscous rupture occurs at progressively higher T_{vr} and after shorter t_{vr}, responding to more rapid crystallization kinetics (Fig. 4 d, e, f; 6; 7 and Table 3). At the viscous

rupture, the suspending melt viscosity values show a minor decrease (from ~ 3.1 to ~ 2.8 log Pa s), with increasing $\dot{\gamma}$ (Fig. 4d; Fig. 6). At the same time, the relative viscosity at the viscous rupture decreases (Fig. 4f and Table 3). According to the viscosity model of Vona et al (2011), the values of η_r at the rupture are reproduced for ϕ variable from ~0.40 to ~0.27 with increasing $\dot{\gamma}$ (Table 3).

As discussed in the previous section, the control of cooling rate on the crystallization kinetics is more effective than that of shear rate (see also Kolzenburg et al., 2018a). With increasing *q*, the onset of crystallization and viscous rupture occurs progressively earlier in time and at lower temperatures (Fig. 4, Fig. 6, Fig. 7 and Table 3). Note that the time and temperature ranges of CDE-*q* experiments are larger than those of CDE-$\dot{\gamma}$, thereby the suspending melt viscosity at viscous rupture increases by one order of magnitude, from 3.1 to 4.1 log Pa s with increasing *q* (Fig. 6). The relative viscosity values calculated at the viscous rupture decrease with increasing *q* (Fig. 4c and Table 3). Analogously, the values of ϕ at the rupture decrease from ~0.34 to ~0.19 as *q* increases (Table 3). This effect is caused by the shorter time spent at *subliquidus* temperature and the more sluggish growth kinetics with increasing melt viscosity.

By comparing CDE-*q* and CDE-$\dot{\gamma}$, it is apparent that the time required to reach the viscous rupture decreases with increasing *q* and $\dot{\gamma}$ (Fig. 7). Moreover, viscous rupture is achieved at lower relative viscosity (Fig. 4 c, f) and, thus, lower crystal fraction. This transition occurs in CDE-$\dot{\gamma}$ within narrow ranges of temperature and suspending melt viscosity, whereas both these parameters change over broader ranges in CDE-*q*, due to the effect of highly variable cooling rate conditions (Fig. 6).

For CDE-$\dot{\gamma}$, it appears that the effects of crystallization on viscosity and the shear rate (higher ϕ and higher η_a at lower $\dot{\gamma}$, and *vice versa*), successfully counterbalance each other,

resulting in viscous rupture at constant τ_{vr} (Fig. 4e). This phenomenon is favored by the narrow range of temperature and suspending melt viscosity over which the ruptures take place. In contrast, for CDE-*q*, the broad variability of *T* and suspending melt viscosity may play a key role on the efficiency of crystal-crystal interaction responsible for the material instabilities and shear localization. In particular, at 5 °C/min, the crystallization process is shifted to low temperatures. Under these conditions, the viscous rupture occurs at the lowest crystal fraction but the highest suspending melt viscosity. We propose that the high suspending melt viscosity hinders crystal movement, aggregation, and shear zone development. In this scenario, the onset of shear localization is delayed and the suspension is more prone to coherent deformation, as supported by the higher threshold τ_{vr}. Cooling rate may also play a key role in this process by controlling crystal growth kinetics and crystal morphology. Indeed, slow cooling rates promote euhedral and prismatic crystal habits, whereas high cooling rates favor the growth of dendritic and skeletal crystals (Logfren, 1980; Zieg and Logfren, 2006; Mollo et al., 2012; Vetere et al., 2015; Kolzenburg et al., 2018a; Pontesilli et al., 2019). As evidenced by post-experimental textures from IDEs, glomerocrysts and leucite-clinopyroxene intergrowths are systematically more abundant with increasing ΔT (Fig. 3). Thus, while the absolute volume fraction of crystals is lower at higher *q*, the effective particle volume (i.e., the volume of skeletal crystals plus the volume of interstitial melt trapped within dendrites) may be equivalent to (or larger than) the volume occupied by euhedral crystals. With increasing *q*, the transition from euhedral to subhedral to anhedral crystal habits may partly facilitate strain localization (e.g., glomerocrysts breakage; Campagnola et al., 2016) and, hence, the viscous rupture at lower crystal contents, as previously suggested by experiments conducted on analog materials (e.g., Soule and Cashman, 2005).

5.4 Mapping the pāhoehoe – ʻaʻā transition

Data presented in Fig. 4 show the effects of q and $\dot{\gamma}$ on the rheological evolution of phonotephritic melt at disequilibrium conditions. This is the first data set that systematically documents the transition from coherent flow to viscous rupture for a natural silicate melt at cooling and shear rate conditions pertinent to lava flow emplacement. Peterson and Tilling (1980) observed that the pāhoehoe – ʻaʻā transition is directly related to the balance between the apparent viscosity of the lava and the shear rate applied to it. Consequently, the transition represents a threshold limit in the effective shear stress that the melt is able to sustain without losing coherence during flow (i.e., "rupturing", according to Kilburn, 1990 and Harris et al., 2017). Therefore, our experimental results shed light on the dynamic processes taking place during lava emplacement and allow to generate a multiparameter map of the pāhoehoe – ʻaʻā transition (Fig. 8a). To date, the pāhoehoe – ʻaʻā transition has been principally investigated by field studies (e.g., Peterson and Tilling, 1980; Cashman et al., 1999; Hon et al., 2003; Lanzafame et al., 2013; Robert et al., 2014; Harris et al., 2020). Quantitative data are scarce and limited to analog and/or isothermal experiments (e.g., Soule and Cashman, 2005; Sehlke et al., 2014; Soldati et al., 2017), which are not directly applicable to the disequilibrium conditions of lava flow emplacement.

The most important outcomes from this study are summarized in Fig. 8a, using the semi-quantitative diagram proposed in Hon et al. (2003). This regime diagram depicts the pāhoehoe – ʻaʻā transition in shear rate – apparent viscosity space, separating the surface expression of the lava based on rheological parameters. The measurements presented here permit to develop a dynamic flow regime diagram, tracking the rheology of lava flow from *superliquidus* condition

(i.e., crystal-free melt) to viscous rupture (i.e., the transition from pāhoehoe to ʻaʻā morphologies).

The transition from pāhoehoe to ʻaʻā morphology (and flow regimes) is not sharp, but occurs through a transitional threshold zone (TTZ; Peterson and Tilling, 1980). We define the transition from coherent flow (pāhoehoe field) to the onset of a clumping regime related to particle-particle interaction (the lower boundary of TTZ; Soule and Cashman, 2005), as the first occurrence of small stress drops in the viscosity measurements (see Fig. 4 and Fig. S5). The final stress drop resulting from viscous rupture in our experiments (Fig. 4 and Fig. S5) defines the boundary for transition to ʻaʻā morphology (i.e., the upper boundary of TTZ). Thus, with increasing viscosity in response to cooling and crystallization, our data identify both the pāhoehoe – TTZ and TTZ – ʻaʻā transitions for a broad range of shear rates, also providing information on the crystal volume fraction.

For CDE-$\dot{\gamma}$, the onset of the clumping regime is evident at $\dot{\gamma}$ ranging from 1 to 5 s^{-1}, but it is less clear at $\dot{\gamma}$ from 10 to 20 s^{-1}. The pāhoehoe – TTZ boundary shifts to higher η_a with decreasing $\dot{\gamma}$, describing the same trend documented for basaltic lavas (Hon et al., 2003; Sehlke et al., 2014; Soldati et al., 2017) and analog materials (Soule and Cashman, 2005) (Fig. 8b). The transition to ʻaʻā morphology (i.e., viscous rupture) also occurs at progressively higher viscosities with decreasing $\dot{\gamma}$ (Fig. 8a). As a result, the TTZ zone becomes wider with decreasing shear rate. The TTZ upper boundary cannot be constrained for the experiment conducted at $\dot{\gamma}$ of 1 s^{-1} as viscous rupture is not observed within the maximum stress limit of the rheometer. At low $\dot{\gamma}$, both the pāhoehoe – TTZ and TTZ – ʻaʻā transition boundaries asymptotically approach 0 s^{-1}. By integrating the experimental data and rheological models, the crystal fraction expected at each transition can be also quantified. In particular, as the shear rate increases, the pāhoehoe -

ʻaʻā transition occurs not only at progressively lower viscosities (as noted in Soule and Cashman, 2005; Sehlke et al., 2014) but also at lower crystal fractions (Fig. 8a). This is likely a result of the fact that higher shear rates i) enhance the particle-particle interaction and ii) influence the shapes of growing crystals (Kouchi et al., 1986; Vona and Romano, 2013; Kolzenburg et al., 2020), promoting shear localization at lower crystal contents. This implies that the crystal fraction at the transition may shift as a function of crystal shape and its effect on the suspension viscosity. The onset of force chain formation is the most likely cause promoting rupture of the suspension below the viscous-brittle transition and further investigation using methods to track the textural evolution of samples during flow (Dobson et al., 2020) will help to delineate more clearly this threshold.

Additionally, our data highlight that the pāhoehoe – ʻaʻā transition is not merely a 2D process governed only by apparent viscosity and shear rate changes but it is also dependent on the imposed cooling rate (Fig. 8a). CDE-*q* experiments were performed at $\dot{\gamma}$ of 5 s^{-1} and thus all data plot along a horizontal line. Pāhoehoe – TTZ and TTZ – ʻaʻā boundaries shift towards higher apparent viscosity values with increasing *q* (see inset in Fig. 8a). This shift is possibly due to the effect of delayed nucleation with increasing cooling rate and the shorter time spent at *subliquidus* temperatures, that limits particle-particle interaction and clumping.

In summary, under disequilibrium conditions representative of several natural lava flow emplacement scenarios, both cooling and deformation rates play a pivotal role in determining the pāhoehoe – ʻaʻā transition (Fig. 9). In particular, the cooling path exerts a first order control on the crystallization kinetics, where lower cooling rates promote crystallization, favoring crystal-crystal interaction, shear localization, and viscous rupture. This reduces the ability of lava to develop a pāhoehoe crust and, thus, enlarges the ʻaʻā flow window (Fig. 8a, 9). The same

processes are activated by advection-enhanced crystallization with increasing shear rates, therefore shifting the TTZ during lava emplacement and triggering the onset of lava rupture and ‘a‘ā propagation (Fig. 8a, 9). Overall, the magnitude of the shear rate effect appears subordinate to that of cooling rate. It should be noted that the presence of a pre-existent crystal cargo (e.g., Lanzafame et al., 2013) could further reduce the pāhoehoe window and promote the transition to ‘a‘ā lava flow.

While the shape and width of the transition zone delineated by our measurements (Fig. 8a) conform to those of previous studies (Hon et al., 2003; Soule and Cashman, 2005; Robert et al., 2014; Sehlke et al., 2014), our experimental results document that the transition zone for phonotephritic melts is shifted by about one order of magnitude towards higher apparent viscosities with respect to previously published data (Fig. 8b). Indeed, earlier studies focused only on the pāhoehoe – ‘a‘ā transition of basaltic lavas by using direct field observations (Hon et al., 2003), high temperature experiments (Sehlke et al., 2014; Soldati et al., 2017), and experiments conducted on analog materials optimized to mimic their interstitial melt viscosity (Soule and Cashman, 2005). Notably, neither changes in melt composition nor environmental conditions (i.e., cooling and/or shear rates) were considered so far. In this context, the results from this study expand the compositional and thermal space over which this transition is investigated, denoting that TTZ is not a static boundary but, instead, a composition-, cooling- and shear-dependent transition zone whose rheological features remain poorly mapped.

6 Conclusions

By integrating Isothermal Deformation Experiments (IDEs) and Cooling Deformation Experiments (CDEs), we have quantified the effects of undercooling, cooling, and shear rates on the crystallization kinetics and rheological evolution of a phonotephritic melt. Our data allow to delineate the viscosity-temperature-time window within which the lava solidifies under both equilibrium and disequilibrium conditions. The melt crystallization path is also determined, in concert with the rheological transition from coherent flow to viscous rupture; thus mapping the pāhoehoe – ʻaʻā transition. Relying on these experimental data, the following conclusions can be drawn:

1) IDEs identify the maximum viscosity limit of crystal-bearing lava under equilibrium crystallization conditions. High initial degrees of undercooling and shear rates both enhance crystallization by reducing the incubation time of nucleation, and promoting the achievement of equilibrium crystal contents;
2) experiments conducted at variable cooling rates and variable shear rates (CDEs) produce disequilibrium crystallization conditions. The crystallization is suppressed at the critical cooling rate of 10 °C/min. At a given temperature, due to delayed nucleation and crystallization kinetics, the melt viscosity is systematically lower than that expected under equilibrium crystal growth conditions;
3) CDE-*q* (variable cooling rate and constant shear rate) showed that cooling rate exerts a first-order control on the rheological evolution of the melt. The onset of crystallization and viscous rupture occur at lower temperature and shorter experimental time with increasing cooling rate. The critical shear stress value at which viscous rupture takes place increases with increasing cooling rate, in response to increasing melt viscosity hindering crystal movement and clustering;

4) CDE-$\dot{\gamma}$ (constant cooling rate and variable shear rate) showed that a shear rate increase enhances the crystallization kinetics of the solidifying melt, resulting in crystallization and viscous rupture at higher temperatures and earlier in time. Viscous rupture occurs at constant values of shear stress, recording a balancing effect between the suspension viscosity and the magnitude of the applied shear rate;
5) direct application of experimental data to pāhoehoe – ʻaʻā transition in natural lava flows indicates that the crystallization is enhanced by decreasing cooling rates and/or increasing shear rates, favoring crystal-crystal interaction, shear localization, and viscous rupture phenomena. This limits the ability of lava flow to develop a pāhoehoe crust, thus favoring and enlarging the ʻaʻā window;
6) the classical 2D regime diagram (viscosity vs. shear rate) of lava flow morphology needs to be refined to include the dependence of pāhoehoe – ʻaʻā transition on cooling rate and disequilibrium crystallization kinetics;
7) comparison with previous studies conducted on basalts demonstrates that under disequilibrium conditions, the viscosity threshold at which pāhoehoe – ʻaʻā transition takes place is not universal, but shows a further dependence on magma bulk composition. This compositional effect, in concert with the control of cooling rate on pāhoehoe – ʻaʻā transition, should be systematically investigated in order to improve our ability to model and forecast lava emplacement and volcanic hazard.

Acknowledgments

This research was funded by: MIUR grants to Roma Tre PhD School in Earth Sciences (XXXIV doctoral cycle). The Grant of Excellence Departments, MIUR-Italy (ARTICOLO 1, COMMI 314 - 337 LEGGE 232/2016) is also gratefully acknowledged. SK acknowledges H2020 Marie Skłodowska-Curie fellowship DYNAVOLC – No.795044. Our manuscript benefited greatly from discussions with G. Iezzi. The authors like to thank the reviewers M. O. Chevrel and R. A. Duraiswami for comments and suggestions that helped to improve this manuscript. We would also like to thank S. Parman (Editor) and the Associate Editor (anonymous) for editorial handling of the manuscript. The authors declare no conflicts of interest. The data archiving is underway on Figshare (the following DOI will become active when the item is published: 10.6084/m9.figshare.14188697).

Figure captions

Figure 1: Schematic diagrams of the apparent viscosity-time paths during crystallization experiments. Diagrams illustrate the viscosity evolution and the related kinetic processes taking place under (a) near-equilibrium (isothermal deformation experiments, IDEs) or (b) disequilibrium (cooling deformation experiments, CDEs) conditions. In (a) four regions can be recognized with increasing experimental time (t). Viscosity initially increases due to thermal relaxation of the melt at the dwell temperature and reaches the time-invariant viscosity of the metastable liquid before crystallization is observed. The length of this plateau reflects the incubation time of crystallization. Subsequently, viscosity increases due to crystallization, until reaching time-invariant viscosity of the crystal-bearing melt with a stable crystal content (i.e., thermomechanical equilibrium). Once a stable crystal content is recognized over time, the rheological measurements are interrupted (redrawn from Vona and Romano, 2013). In (b) the measured apparent viscosity initially follows the viscosity-temperature path of the pure liquid at *superliquidus* temperatures (provided that the cooling rate is sufficiently slow to allow the thermal relaxation of the melt). Once the temperature decreases below the *liquidus* conditions and the melt is driven into an undercooled regime, this initial trend continues over the incubation phase until the suspension crystallinity is sufficiently high to affect the rheology of the system. At this point, the measured viscosity deviates from the theoretical viscosity-temperature path of the crystal-free liquid and the magnitude of viscosity progressively increases. This departure is more effective with increasing undercooling and measurements typically terminate once the torque limit of the rheometer is reached or manually interrupted after a stress drop (indicative of viscous rupture) is observed.

Figure 2: Summary of IDE data. (a) Temporal evolution of viscosity. PoX15 (T = 1,189 °C), PoX17 (T = 1,178 °C), and PoX18 (T = 1,168 °C) were run at $\dot{\gamma}$ of 1 s^{-1}, whilst PoX19 (T = 1,167 °C) was run at $\dot{\gamma}$ of 3 s^{-1} (see Table 2). See Fig. 1a for the interpretation of the kinetic processes. The inset shows the shear rate dependence of the suspension viscosity measured at stable conditions for $\dot{\gamma}$ ranging between 3 and 0.1 s^{-1}. (b) The effect of crystal fraction on the rheology of phonotephrite melt. The symbol size reflects the observed non-Newtonian behavior and the uncertainty in crystal content determination (Fig. 2a inset and Fig. S3). Grey fields outline relative viscosity estimates using the model of Vona et al. (2011) for crystal-bearing magma/lava viscosity, crystal mean aspect ratio R of 1, 2, 3, and 4 for shear rate of $1 \leq \dot{\gamma} \leq 3$ s^{-1}.

Figure 3: Results of textural analysis of IDEs (see details in Table 2). (a-d) BSE images collected at magnification of 120x. The mineral assemblage consists of leucite (dark grey) and clinopyroxene (light grey) in a glassy matrix (intermediate grey tone). (e-h) Crystal Volume Distribution (CVD) diagrams showing stacked histograms of crystal size vs. volume fraction of leucite and clinopyroxene.

Figure 4: Summary of CDEs data. a) Viscosity-temperature measurements of CDE-q, performed at constant $\dot{\gamma}$ of 5 s^{-1} and q of 1, 3 5, and 10 °C/min. CDE-q data are also expressed as b) shear stress (τ) vs. temperature and c) relative viscosity (η_r) vs. temperature. d) Viscosity-temperature measurements of CDE-$\dot{\gamma}$, performed at constant q of 1 °C/min and $\dot{\gamma}$ of 1, 2.5, 5, 10, and 20 s^{-1}.

CDE-$\dot{\gamma}$ data are also expressed as e) shear stress (τ) vs. temperature and f) relative viscosity (η_r) vs. temperature. In all diagrams, the experiment performed at $\dot{\gamma}$ of 5 s^{-1} and q of 1 °C/min (belonging to both CDE-q and CDE-$\dot{\gamma}$ data sets) is colored in red to facilitate cross comparison. The dashed line in a) and d) represents the VFT modeling of the pure melt viscosity.

Figure 5: Surface morphologies of representative post-experimental samples. a) Sketch of concentric cylinder geometry (for scale). b) Post-experiment surface morphology of the sample recovered at the end of the crystal-free melt viscosity measurement (see Section 4.1). Note that the spindle was not removed before quenching and the spiral-shaped flow lines are clearly visible. c, d) Post-experiment surface morphology of the sample recovered at the end of CDEs by quenching in water (c) or after complete solidification (d). Note that the hole (localizing the spindle position) is slightly offset from the original central position in (c). In (d), leucite crystals forming aggregates are recognizable as green spots.

Figure 6: Viscosity-temperature regime diagram for phonotephritic melts at P = 1 atm and fO_2 = air. The rheological evolution of the melt upon crystallization is bounded by two threshold limits: i) equilibrium crystallization (maximum viscosity) and ii) suppressed crystallization (minimum viscosity). The upper limit (thick gray area) is derived by MELTS thermodynamic simulations (Ghiorso and Sack, 1995; Asimow and Ghiorso, 1998; $T_{liquidus}$ of 1273 °C corresponding to the star symbol) and rheological modeling (Vona et al., 2011) for variable H_2O content and R of crystalline phases (see text). This boundary is in good agreement with IDE data (black empty symbols; with vertical lines showing the small non-Newtonian behavior observed; Fig. 2a inset). The lower limit is defined by the crystal-free melt viscosity. In this context, both the onset of crystallization and viscous rupture can be traced for disequilibrium experiments (i.e., filled circles for CDE-q and green solid/empty symbols for CDE-$\dot{\gamma}$). For CDE-q of 10 °C/min showing no crystallization, the symbol represents the final viscosity value at which the experiment was interrupted.

Figure 7: Time-temperature-transformation (TTT) diagram of phonotephrite melts at P = 1 atm and fO_2 = air. Effect of cooling paths on the crystallization process and related rheological evolution for CDE-q (a) and CDE-$\dot{\gamma}$ (b). Dashed lines correspond to cooling rates of 1 °C/min (green), 3 °C/min (red), 5 °C/min (blue) and 10 °C/min (black). In (a) the black rectangle indicates the area blown up in (b) to highlight the effect of shear rate at constant q (CDE-$\dot{\gamma}$). In (b) the experiment conducted at $\dot{\gamma}$ = 5 s^{-1} (green circles) is plotted in all diagrams for comparison.

Figure 8: Diagram of shear rate vs. apparent viscosity of lava flows. a) Shaded area is the "transition threshold zone" (TTZ), which separates the pāhoehoe and ʻaʻā flow regimes (Peterson and Tilling, 1980). CDE-$\dot{\gamma}$ data (green filled and empty symbols) are displayed in the main diagram and are used to define the TTZ boundaries. The black dashed rectangle indicates the zoom-in areas in the inset, showing the modification of TTZ in response to different cooling rates (i.e., CDE-q data showed as filled circles). CDE data are depicted as continuous straight lines (i.e., yellow and orange lines for crystal-free melt and melt + crystals, respectively), representing the viscosity path

of the melt at constant shear rate. Numbers at the end of each straight line indicate the crystal fraction estimated at viscous rupture, with the exception of the experiment at 1 s-1 where the value represents the maximum crystal fraction at the rheometer torque limit. For this case, the TTZ upper limit is uncertain. Analogously, question marks along the TTZ lower limit indicate the inferred threshold values that were not clearly recognizable from the viscosity path (Fig. S5). b) TTZ fields from this study and previous literature data separating pāhoehoe and ʻaʻā morphologies. Literature data are mostly based on basalts and refer to experiments on analog (Soule and Cashman, 2005) and natural (Sehlke et al. 2014; Soldati et al., 2017) materials, as well as direct observations and measurements on active lava flows (Hon et al., 2003).

Figure 9: Conceptual model of the pāhoehoe-ʻaʻā transition processes. a) Schematic sketch of the morphologies and flow-type zones produced by different rheological responses of lava flow (from coherent viscous flow to autobrecciation). The colored bars represent the shift of pahoehoe, TTZ and ʻaʻā zones as a function of cooling and shear rates. White hexagons and black elongate shapes show the progressive formation and clustering of crystals with different aspect ratios up to the point of enhanced shear localization. b), c) and d) show the comparison between morphologies of natural lava and those of experimental samples. b) Field appearance of pāhoehoe lava flow emplaced as lobes and toes (Hawaii, Kilauea, 61G flow, Nov. 2016; photo courtesy of M. O. Chevrel); c) Field appearance of a lava flow breakout with a transitional pāhoehoe to ʻaʻā surface morphology (Holuhraun, Iceland, November 2014; photo by S. Kolzenburg); d) ʻAʻā lava flow front (Holuhraun, Iceland, November 2014; photo by S. Kolzenburg).

References

Arzilli, F., La Spina, G., Burton, M. R., Polacci, M., Le Gall, N., Hartley, M. E., Di Genova, D., Cai, B., Vo, N. T., Bamber, E. C., Nonni, S., Atwood, R., Llewellin, E. W., Brooker, R. A., Mader, H. M., & Lee, P. D. (2019). Magma fragmentation in highly explosive basaltic eruptions induced by rapid crystallization. Nature Geoscience, 12(12), 1023–1028. https://doi.org/10.1038/s41561-019-0468-6

Asimow, P. D., & Ghiorso, M. S. (1998). Algorithmic modifications extending MELTS to calculate subsolidus phase relations. American Mineralogist, 83(9–10), 1127–1132. https://doi.org/10.2138/am-1998-9-1022

Behrens, H., & Gaillard, F. (2006). Geochemical aspects of melts: Volatiles and redox behavior. Elements, 2(5), 275–280. https://doi.org/10.2113/gselements.2.5.275

Belkin, H. E., Kilburn, C. R. J., & Vivo, B. De. (1993). Sampling and major element chemistry of the recent (A.D. 1631-1944) Vesuvius activity, 58, 273–290.

Calabrò, L., Harris, A. J. L., & Thouret, J. C. (2020). Media views of the Stromboli 2002-2003 eruption and evacuation: A content analysis to understand framing of risk communication during a volcanic crisis. Journal of Applied Volcanology, 9(1). https://doi.org/10.1186/s13617-020-00094-0

Campagnola, S., Vona, A., Romano, C., & Giordano, G. (2016). Crystallization kinetics and rheology of leucite-bearing tephriphonolite magmas from the Colli Albani volcano (Italy). Chemical Geology, 424, 12–29. https://doi.org/10.1016/j.chemgeo.2016.01.012

Cashman, K. V, & Blundy, J. D. (2000). Degassing and crystallization of ascending andesite and dacite. Philosophical Transaction of the Royal Society of London A 358, 1487–1513

Cashman, K. V., Thornber, C., & Kauahikaua, J. P. (1999). Cooling and crystallization of lava in open channels, and the transition of Pāhoehoe Lava to ʼAʻā. Bulletin of Volcanology 61, 306–323.

Chevrel, M. O., Pinkerton, H., & Harris, A. J. L. (2019). Measuring the viscosity of lava in the field: A review. Earth-Science Reviews, 196(May). https://doi.org/10.1016/j.earscirev.2019.04.024

Chevrel, M. O., Harris, A. J. L., James, M. R., Calabrò, L., Gurioli, L., & Pinkerton, H. (2018). The viscosity of pāhoehoe lava: In situ syn-eruptive measurements from Kilauea, Hawaii. Earth and Planetary Science Letters, 493, 161–171. https://doi.org/10.1016/j.epsl.2018.04.028

Chevrel, M. O., Cimarelli, C., & Hanson, J. (2015). Viscosity measurements of crystallizing andesite from Tungurahua volcano (Ecuador). Geochemistry Geophysics Geosystems 16, 870–889. Available at: http://dx.doi.org/10.1002/2014GC005661

Chevrel, M. O., Platz, T., Hauber, E., Baratoux, D., Lavallée, Y., & Dingwell, D. B. (2013). Lava flow rheology: A comparison of morphological and petrological methods. Earth and Planetary Science Letters, 384, 109–120. https://doi.org/10.1016/j.epsl.2013.09.022

Cordonnier, B., Lev, E., & Garel, F. (2016). Benchmarking lava-flow models eds. A. J. L. Harris, T. De Groeve, F. Garel, and S. A. Carn. Detecting Modelling and Responding to Effusive Eruptions, 426, 0. Available at: https://doi.org/10.1144/SP426.7.

Cordonnier, B., Caricchi, L., Pistone, M., Castro, J., Hess, K. U., Gottschaller, S., et al. (2012). The viscous-brittle transition of crystal-bearing silicic melt: Direct observation of magma rupture and healing. Geology, 40(7), 611–614. https://doi.org/10.1130/G3914.1

Di Genova, D., Sicola, S., Romano, C., Vona, A., Fanara, S., & Spina, L. (2017). Effect of iron and nanolites on Raman spectra of volcanic glasses: A reassessment of existing strategies to estimate the water content. *Chemical Geology*, *475*(June), 76–86. https://doi.org/10.1016/j.chemgeo.2017.10.035

Di Genova, D., Romano, C., Giordano, D., & Alletti, M. (2014). Heat capacity, configurational heat capacity and fragility of hydrous magmas. Geochimica et Cosmochimica Acta, 142, 314–333. https://doi.org/10.1016/j.gca.2014.07.012

Dingwell, D. B. (1996). Volcanic dilemma: Flow or blow? Science, 273(5278), 1054–1055. https://doi.org/10.1126/science.273.5278.1054

Dingwell, D. B. (1986). Viscosity-temperature relationships in the system Na2Si2O5-Na4Al2O5. Geochimica et Cosmochimica Acta, 50(6), 1261–1265. https://doi.org/10.1016/0016-7037(86)90409-6

Dobson, K.J., Allabar, A., Bretagne, E., Coumans, J., Cassidy, M., Cimarelli, C., Coats, R., Connolley, T., Courtois, L., Dingwell, D.B., Di Genova, D., Fernando, B., Fife, J.L., Fyfe, F., Gehne, S., Jones, T., Kendrick, J.E., Kinvig, H., Kolzenburg, S., Lavallée, Y., Liu, E., Llewellin, E.W., Madden-Nadeau, A., Madi, K., Marone, F., Morgan, C., Oppenheimer, J., Ploszajski, A., Reid, G., Schauroth, J., Schlepütz, C.M., Sellick, C., Vasseur, J., von Aulock, F.W., Wadsworth, F.B., Wiesmaier, S., & Wanelik, K. (2020). Quantifying Microstructural Evolution in Moving Magma. Frontiers in Earth Science, 8,1–22. https://doi.org/10.3389/feart.2020.00287

Dragoni, M., & Tallarico, A. (1994). The effect of crystallization on the rheology and dynamics of lava flows. Journal of Volcanology and Geothermal Research, 59(3), 241–252. https://doi.org/10.1016/0377-0273(94)90098-1

Duraiswami, R. A., Gadpallu, P., Shaikh, T. N., & Cardin, N. (2014). Pahoehoe-a'a transitions in the lava flow fields of the western Deccan Traps, India-implications for emplacement dynamics, flood basalt architecture and volcanic stratigraphy. *Journal of Asian Earth Sciences*, *84*, 146–166. https://doi.org/10.1016/j.jseaes.2013.08.025

Dutton, C.E., (1884). Hawaiian volcanoes. In: Powell, J.W. (Ed.), Fourth Annual Report of the United States Geological Survey to the Secretary of the Interior, 1882–'83. Government Printing Office, Washington, D.C., pp. 75–219.

Emerson, O. H. (1926). The formation of aa and pahoehoe. American Journal of Science. https://doi.org/10.2475/ajs.s5-12.68.109

Getson, J. M., & Whittington, A. G. (2007). Liquid and magma viscosity in the anorthite-forsterite-diopside-quartz system and implications for the viscosity-temperature paths of cooling magmas. Journal of Geophysical Research: Solid Earth, 112(10), 1–19. https://doi.org/10.1029/2006JB004812

Ghiorso, M. S., & Sack, O. (1995). Chemical mass transfer in magmatic processes. IV: A revised and internally consistent thermodynamic model for the interpolation and extrapolation of

liquid-solid equilibria in magmatic systems at elevated temperatures and pressures. Contributions to Mineralogy and Petrology, 119, 197–212.

Giordano, D., Russell, J. K., & Dingwell, D. B. (2008). Viscosity of magmatic liquids: A model. Earth and Planetary Science Letters, 271(1–4), 123–134. https://doi.org/10.1016/j.epsl.2008.03.038

Giordano, D., Polacci, M., Longo, A., Papale, P., Dingwell, D. B., Boschi, E., & Kasereka, M. (2007). Thermo-rheological magma control on the impact of highly fluid lava flows at Mt. Nyiragongo. Geophysical Research Letters, 34(6), 2–5. https://doi.org/10.1029/2006GL028459

Giuliani, L., Iezzi, G., Vetere, F., Behrens, H., Mollo, S., Cauti, F., et al. (2020). Evolution of textures, crystal size distributions and growth rates of plagioclase, clinopyroxene and spinel crystallized at variable cooling rates from a mid-ocean ridge basaltic melt. Earth-Science Reviews, 204(December 2019), 103165. https://doi.org/10.1016/j.earscirev.2020.103165

Gonnermann, H. M. (2015). Magma Fragmentation. Annual Review of Earth and Planetary Sciences, 43(1), 431–458. https://doi.org/10.1146/annurev-earth-060614-105206

Gonnermann, H. M., & Manga, M. (2007). The fluid mechanics inside a volcano. Annual Review of Fluid Mechanics, 39, 321–356. https://doi.org/10.1146/annurev.fluid.39.050905.110207

Hammer, J. E. (2008). Experimental studies of the kinetics and energetics of magma crystallization. Reviews in Mineralogy and Geochemistry, 69(4), 9–59. https://doi.org/10.2138/rmg.2008.69.2

Hammer, J. E. (2006). Influence of fO2 and cooling rate on the kinetics and energetics of Fe-rich basalt crystallization. Earth and Planetary Science Letters, 248(3–4), 618–637. https://doi.org/10.1016/j.epsl.2006.04.022

Harris, A., Mannini, S., Thivet, S., Chevrel, M. O., Gurioli, L., Villeneuve, N., et al. (2020). How shear helps lava to flow. Geology, 48(2), 154–158. https://doi.org/10.1130/G47110.1

Harris, A. J. L., Rowland, S. K., Villeneuve, N., & Thordarson, T. (2017). Pāhoehoe, ʻaʻā, and block lava: an illustrated history of the nomenclature. Bulletin of Volcanology (Vol. 79) https://doi.org/10.1007/s00445-016-1075-7

Harris, A. J. L., & Rowland, S. K. (2001). FLOWGO: a kinematic thermo-rheological model for lava flowing in a channel. Bulletin of Volcanology, 63, 20–44. https://doi.org/10.1007/s004450000120

Hon, K., Gansecki, C., & Kauahikaua, J. (2003). The transition from ʼAʼā to pāhoehoe crust on flows emplaced during the Puʻu ʻŌʻō-Kūpaianaha eruption. US Geological Survey Professional Paper, (1676), 89–103.

Hoover, S. R., Cashman, K. V., & Manga, M. (2001). The yield strength of subliquidus basalts - Experimental results. Journal of Volcanology and Geothermal Research, 107(1–3), 1–18. https://doi.org/10.1016/S0377-0273(00)00317-6

Huppert, H. E., Sparks, R. S. J., Turner, J. S., & Arndt, N. T. (1984). Emplacement and cooling of komatiite lavas. Nature, 309, 19–22. Available at: https://doi.org/10.1038/309019a0

Iezzi, G., Mollo, S., Shahini, E., Cavallo, A., & Scarlato, P. (2014). The cooling kinetics of plagioclase feldspar as revealed by electron-microprobe mapping. American Mineralogist, 99(5–6), 898–907. https://doi.org/10.2138/am.2014.4626

Iezzi, G., Mollo, S., Ventura, G., Cavallo, A., & Romano, C. (2008). Experimental solidification of anhydrous latitic and trachytic melts at different cooling rates: The role of nucleation kinetics. Chemical Geology, 253(3–4), 91–101. https://doi.org/10.1016/j.chemgeo.2008.04.008

Ishibashi, H. (2009). Non-Newtonian behavior of plagioclase-bearing basaltic magma: Subliquidus viscosity measurement of the 1707 basalt of Fuji volcano, Japan. Journal of Volcanology and Geothermal Research, 181(1–2), 78–88. https://doi.org/10.1016/j.jvolgeores.2009.01.004

Ishibashi, H., & Sato, H. (2007). Viscosity measurements of subliquidus magmas: Alkali olivine basalt from the Higashi-Matsuura district, Southwest Japan. Journal of Volcanology and Geothermal Research, 160(3–4), 223–238. https://doi.org/10.1016/j.jvolgeores.2006.10.001

Jones, T. J., Reynolds, C. D., & Boothroyd, S. C (2019). Fluid dynamic induced break-up during volcanic eruptions. Nature Communications, 10, 1–7. Available at: http://dx.doi.org/10.1038/s41467-019-11750-4.

Kilburn, C.R.J. (2004). Fracturing as a quantitative indicator of lava flow dynamics. J Journal of Volcanology and Geothermal Research, 132, 209–224.

Kilburn, C.R.J. (1990). Surfaces of aa flow-fields on Mount Etna, Sicily; morphology, rheology, crystallization and scaling phenomena, in Fink, J.H., ed., Lava flows and domes; emplacement mechanisms and hazard implications: Berlin, Springer-Verlag, p. 129–156.

Kolzenburg, S., Chevrel, M. O., Dingwell, D. B. (2021). Magma / Suspension Rheology; Reviews in Mineralogy & Geochemistry Vol. 86. Chapter 15. http://dx.doi.org/10.2138/rmg.2020.86.X

Kolzenburg, S., Hess, K., Berlo, K., & Dingwell, D. B. (2020). Disequilibrium Rheology and Crystallization Kinetics of Basalts and Implications for the Phlegrean Volcanic District, 8(June). https://doi.org/10.3389/feart.2020.00187

Kolzenburg, S., Di Genova, D., Giordano, D., Hess, K. U., & Dingwell, D. B. (2018a). The effect of oxygen fugacity on the rheological evolution of crystallizing basaltic melts. Earth and Planetary Science Letters, 487, 21–32. https://doi.org/10.1016/j.epsl.2018.01.023

Kolzenburg, S., Giordano, D., Hess, K. U., & Dingwell, D. B. (2018b). Shear Rate-Dependent Disequilibrium Rheology and Dynamics of Basalt Solidification. Geophysical Research Letters, 45(13), 6466–6475. https://doi.org/10.1029/2018GL077799

Kolzenburg, S., Giordano, D., Thordarson, T., Höskuldsson, A., & Dingwell, D. B. (2017). The rheological evolution of the 2014/2015 eruption at Holuhraun, central Iceland. Bulletin of Volcanology, 79(6). https://doi.org/10.1007/s00445-017-1128-6

Kolzenburg, S., Giordano, D., Cimarelli, C., & Dingwell, D. B. (2016). In situ thermal characterization of cooling/crystallizing lavas during rheology measurements and implications for lava flow emplacement. Geochimica et Cosmochimica Acta, 195, 244–258. https://doi.org/10.1016/j.gca.2016.09.022

Kouchi, A., Tsuchiyama, A., & Sunagawa, I. (1986). Effect of stirring on crystallization kinetics of basalt: texture and element partitioning. Contributions to Mineralogy and Petrology, 93(4), 429–438. https://doi.org/10.1007/BF00371713

La Spina, G., Burton, M., De'Michieli Vitturi, M., & Arzilli, F. (2016). Role of syn-eruptive plagioclase disequilibrium crystallization in basaltic magma ascent dynamics. Nature Communications, 7. https://doi.org/10.1038/ncomms13402

La Spina, G., Burton, M., & de' Michieli Vitturi, M. (2015). Temperature evolution during magma ascent in basaltic effusive eruptions: A numerical application to Stromboli volcano. Earth and Planetary Science Letters, 426, 89–100. https://doi.org/10.1016/j.epsl.2015.06.015

Lanzafame, G., Mollo, S., Iezzi, G., Ferlito, C., & Ventura, G. (2013). Unraveling the solidification path of a pahoehoe "cicirara" lava from Mount Etna volcano. Bulletin of Volcanology, 75(4), 1–16. https://doi.org/10.1007/s00445-013-0703-8

Lofgren, G. (1980). Experimental studies on the dynamic crystallization of silicate melt. In: Hargraves, R. B. (ed.) Physics of Magmatic Processes. Princeton, NJ: Princeton University Press, pp. 487-565.

Mader, H. M., Llewellin, E. W., & Mueller, S. P. (2013). The rheology of two-phase magmas: A review and analysis. Journal of Volcanology and Geothermal Research, 257, 135–158. https://doi.org/10.1016/j.jvolgeores.2013.02.014

Meerlender, G. (1974). Viskositäts-Temperaturverhalten des Standardglases I der DGG" (DGG - Deutsche Glastechnische Gesellschaft, German Society of Glass Technology); Glastechn. Ber., vol. 47.1, p 1-3

Moitra, P., Gonnermann, H. M., Houghton, B. F., & Tiwary, C. S. (2018). Fragmentation and Plinian eruption of crystallizing basaltic magma. Earth Planetary Science Letters, 500, 97–104. Available at: https://doi.org/10.1016/j.epsl.2018.08.003.

Mollo, S., & Hammer, J. E. (2017). Dynamic crystallization in magmas. European Mineralogical Union Notes in Mineralogy, 16, 373–418. https://doi.org/10.1180/EMU-notes.16.12

Mollo, S., & Masotta, M. (2014). Optimizing pre-eruptive temperature estimates in thermally and chemically zoned magma chambers. Chemical Geology, 368, 97–103. https://doi.org/10.1016/j.chemgeo.2014.01.007

Mollo, S., Putirka, K., Misiti, V., Soligo, M., & Scarlato, P. (2013). A new test for equilibrium based on clinopyroxene-melt pairs: Clues on the solidification temperatures of Etnean alkaline melts at post-eruptive conditions. Chemical Geology, 352, 92–100. https://doi.org/10.1016/j.chemgeo.2013.05.026

Mollo, S., Misiti, V., Scarlato, P., & Soligo, M. (2012). The role of cooling rate in the origin of high temperature phases at the chilled margin of magmatic intrusions. Chemical Geology, 322–323, 28–46. https://doi.org/10.1016/j.chemgeo.2012.05.029

Morgan, D. J., & Jerram, D. A. (2006). On estimating crystal shape for crystal size distribution analysis. Journal of Volcanology and Geothermal Research, 154(1–2), 1–7. https://doi.org/10.1016/j.jvolgeores.2005.09.016

Morrison, A., Whittington, A., Smets, B., Kervyn, M., & Sehlke, A. (2020). The rheology of crystallizing basaltic lavas from Nyiragongo and Nyamuragira volcanoes, D.R.C. Volcanica, 3(1), 1–28. https://doi.org/10.30909/vol.03.01.0128

Papale, P. (1999). Strain-induced magma fragmentation in explosive eruptions. Nature, 397(6718), 425–428. https://doi.org/10.1038/17109

Peterson, D. W., & Tilling, R. I. (1980). Transition of basaltic lava from pahoehoe to aa, Kilauea Volcano, Hawaii: Field observations and key factors. Journal of Volcanology and Geothermal Research, 7(3–4), 271–293. https://doi.org/10.1016/0377-0273(80)90033-5

Pinkerton, H., & Norton, G. (1995). Rheological properties of basaltic lavas at sub-liquidus temperatures: laboratory and field measurements on lavas from Mount Etna. Journal of Volcanology and Geothermal Research, 68(4), 307–323. https://doi.org/10.1016/0377-0273(95)00018-7

Pontesilli, A., Masotta, M., Nazzari, M., Mollo, S., Armienti, P., Scarlato, P., & Brenna, M. (2019). Crystallization kinetics of clinopyroxene and titanomagnetite growing from a trachybasaltic melt: New insights from isothermal time-series experiments. Chemical Geology, 510(September 2018), 113–129. https://doi.org/10.1016/j.chemgeo.2019.02.015

Ramsey, M.S., Chevrel, M.O., Coppola, D., & Harris, A.J.L. (2019). The influence of emissivity on the thermo-rheological modeling of the channelized lava flows at tolbachik volcano. Annals of Geophysics, 62, 1–24. https://doi.org/10.4401/ag-8077

Robert, B., Harris, A., Gurioli, L., Médard, E., Sehlke, A., & Whittington, A. (2014). Textural and rheological evolution of basalt flowing down a lava channel. Bulletin of Volcanology, 76(6), 1–21. https://doi.org/10.1007/s00445-014-0824-8

Rusiecka, M. K., Bilodeau, M., & Baker, D. R. (2020). Quantification of nucleation delay in magmatic systems: experimental and theoretical approach. Contributions to Mineralogy and Petrology, 175(5), 1–16. https://doi.org/10.1007/s00410-020-01682-4

Saar, M. O., & Manga, M. (2002). Continuum percolation for randomly oriented soft-core prisms. Physical Review E - Statistical Physics, Plasmas, Fluids, and Related Interdisciplinary Topics, 65(5), 6. https://doi.org/10.1103/PhysRevE.65.056131

Saar, M. O., Manga, M., Cashman, K. V., & Fremouw, S. (2001). Numerical models of the onset of yield strength in crystal-melt suspensions. Earth and Planetary Science Letters, 187(3–4), 367–379. https://doi.org/10.1016/S0012-821X(01)00289-8

Sable, J. E., Houghton, B. F., Del Carlo, P., & Coltelli, M. (2006). Changing conditions of magma ascent and fragmentation during the Etna 122 BC basaltic Plinian eruption: Evidence from clast microtextures. Journal of Volcanology and Geothermal Research, 158, 333–354. Available at: http://linkinghub.elsevier.com/retrieve/pii/S0377027306003222.

Sato, H. (2005). Viscosity measurement of subliquidus magmas: 1707 basalt of Fuji volcano. Journal of Mineralogical and Petrological Sciences, 100(4), 133–142. https://doi.org/10.2465/jmps.100.133

Sehlke, A., & Whittington, A. G. (2020). Rheology of a KREEP analog magma: Experimental results applied to dike ascent through the lunar crust. Planetary and Space Science, 187(April), 104941. https://doi.org/10.1016/j.pss.2020.104941

Sehlke, A., Whittington, A., Robert, B., Harris, A., Gurioli, L., Médard, E., & Sehlke, A. (2014). Pahoehoe to áá transition of Hawaiian lavas: An experimental study. Bulletin of Volcanology, 76(11). https://doi.org/10.1007/s00445-014-0876-9

Soldati, A., Beem, J., Gomez, F., Huntley, J. W., Robertson, T., & Whittington, A. (2017). Emplacement dynamics and timescale of a Holocene flow from the Cima Volcanic Field (CA): Insights from rheology and morphology. Journal of Volcanology and Geothermal Research, 347, 91–111. https://doi.org/10.1016/j.jvolgeores.2017.09.005

Soldati, A., Sehlke, A., Chigna, G., & Whittington, A. (2016). Field and experimental constraints on the rheology of arc basaltic lavas: the January 2014 Eruption of Pacaya (Guatemala). Bulletin of Volcanology, 78(6). https://doi.org/10.1007/s00445-016-1031-6

Soule, S. A., & Cashman, K. V. (2005). Shear rate dependence of the pāhoehoe-to-'a 'ā transition: Analog experiments. Geology, 33(5), 361–364. https://doi.org/10.1130/G21269.1

Stein, D.J., & Spera, F.J. (1998). New high-temperature rotational rheometer for silicate melts, magmatic suspensions, and emulsions. Reviews of Scientific Instruments, 69, 3398–3402. https://doi.org/10.1063/1.1149106.

Sulpizio, R., Mele, D., Dellino, P., & La Volpe, L. (2005). A complex, Subplinian-type eruption from low-viscosity, phonolitic to tephri-phonolitic magma: The AD 472 (Pollena) eruption of Somma-Vesuvius, Italy. Bulletin of Volcanology, 67(8), 743–767. https://doi.org/10.1007/s00445-005-0414-x

Tammann, G., & Hesse, W. (1926). Die Abhängigkeit der Viskosität von der Temperatur bei unterkühlten Flüssigkeiten. Zeitschrift für anorganische und allgemeine Chemie, 156, 245–257.

Tripoli, B., Manga, M., Mayeux, J., & Barnard, H. (2019). The Effects of Deformation on the Early Crystallization Kinetics of Basaltic Magmas. Frontiers in Earth Science, 7, 250. Available at: https://doi.org/10.3389/feart.2019.00250

Vetere, F., Mazzeo, A., Perugini, D., & Holtz, F. (2020). Viscosity behaviour of silicate melts during cooling under variable shear rates. Journal of Non-Crystalline Solids, 533(December 2019), 119902. https://doi.org/10.1016/j.jnoncrysol.2020.119902

Vetere, F., Murri, M., Alvaro, M., Domeneghetti, M.C., Rossi, S., Pisello, A., Perugini, D., & Holtz, F. (2019). Viscosity of Pyroxenite Melt and Its Evolution During Cooling. Journal of Geophysical Research: Planets, 124, 1451–1469. https://doi.org/10.1029/2018JE005851

Vetere, F., Rossi, S., Namur, O., Morgavi, D., Misiti, V., Mancinelli, P., Petrelli, M., Pauselli, C., & Perugini, D. (2017). Experimental constraints on the rheology, eruption, and

emplacement dynamics of analog lavas comparable to Mercury's northern volcanic plains. Journal of Geophysical Research: Planets, 122, 1522–1538.

Vetere, F., Iezzi, G., Behrens, H., Holtz, F., Ventura, G., Misiti, V., et al. (2015). Glass forming ability and crystallisation behaviour of sub-alkaline silicate melts. Earth-Science Reviews, 150, 25–44. https://doi.org/10.1016/j.earscirev.2015.07.001

Vetere, F., Sato, H., Ishibashi, H., De Rosa, R., & Donato, P. (2013a). Viscosity changes during crystallization of a shoshonitic magma: New insights on lava flow emplacement. Journal of Mineralogical and Petrological Sciences, 108(3), 144–160. https://doi.org/10.2465/jmps.120724

Vetere, F., Iezzi, G., Behrens, H., Cavallo, A., Misiti, V., Dietrich, M., Knipping, J., Ventura, G., & Mollo, S. (2013b). Intrinsic solidification behaviour of basaltic to rhyolitic melts: A cooling rate experimental study. Chemical Geology, 354, 233–242. https://doi.org/10.1016/j.chemgeo.2013.06.007

Vona, A., Romano, C., Giordano, G., & Sulpizio, R. (2020). Linking magma texture, rheology and eruptive style during the 472 AD Pollena Subplinian eruption (Somma-Vesuvius). Lithos, 370–371, 105658. https://doi.org/10.1016/j.lithos.2020.105658

Vona, A., Di Piazza, A., Nicotra, E., Romano, C., Viccaro, M., & Giordano, G. (2017). The complex rheology of megacryst-rich magmas: The case of the mugearitic "cicirara" lavas of Mt. Etna volcano. Chemical Geology, 458, 48–67. https://doi.org/10.1016/j.chemgeo.2017.03.029

Vona, A., & Romano, C. (2013). The effects of undercooling and deformation rates on the crystallization kinetics of Stromboli and Etna basalts. Contributions to Mineralogy and Petrology, 166(2), 491–509. https://doi.org/10.1007/s00410-013-0887-0

Vona, A., Romano, C., Dingwell, D. B., & Giordano, D. (2011). The rheology of crystal-bearing basaltic magmas from Stromboli and Etna. Geochimica et Cosmochimica Acta, 75(11), 3214–3236. https://doi.org/10.1016/j.gca.2011.03.031

Webb, S. L., & Dingwell, D. B. (1990). The onset of non-Newtonian rheology of silicate melts - A fiber elongation study. Physics and Chemistry of Minerals, 17, 125–132.

Whittington, A. G., Richet, P., & Polian, A. (2012). Water and the compressibility of silicate glasses: A Brillouin spectroscopic study. American Mineralogist, 97, 455–467. Available at: http://ammin.geoscienceworld.org/cgi/doi/10.2138/am.2012.3891.

Zieg, M.J., & Lofgren, G.E. (2006). An experimental investigation of texture evolution during continuous cooling. Journal of Volcanology and Geothermal Research, 154: 74–88

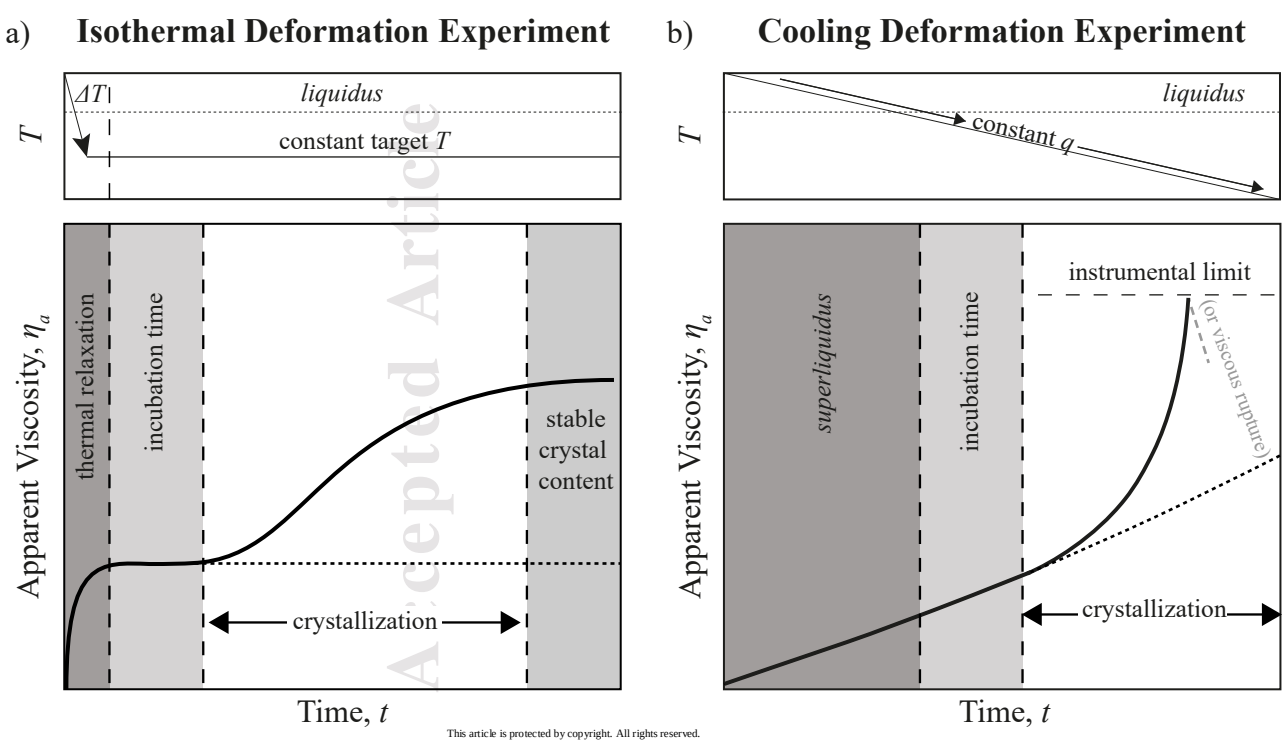

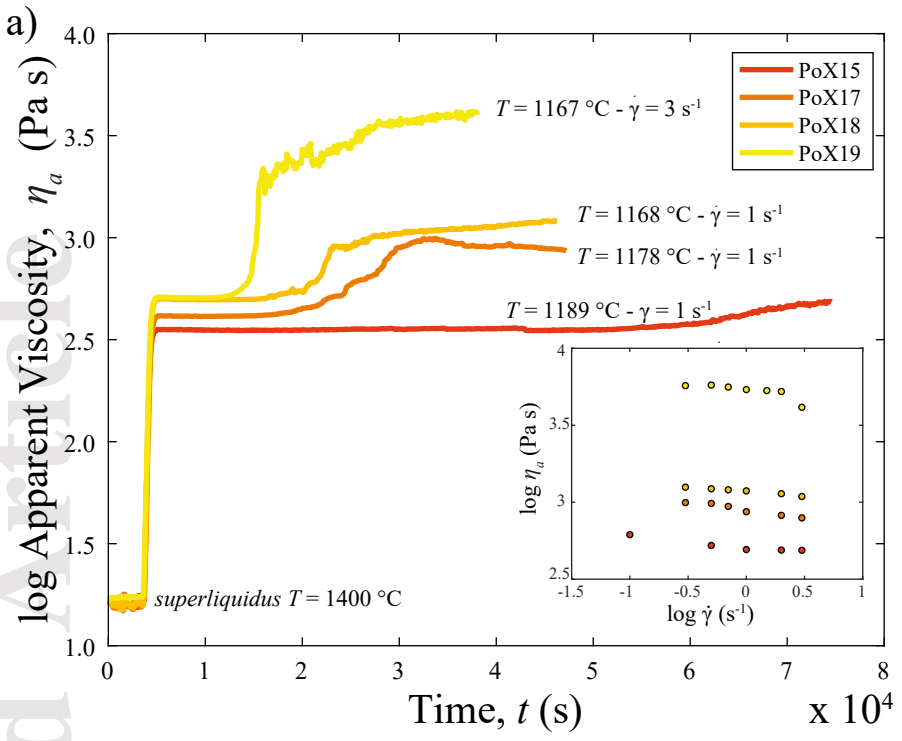

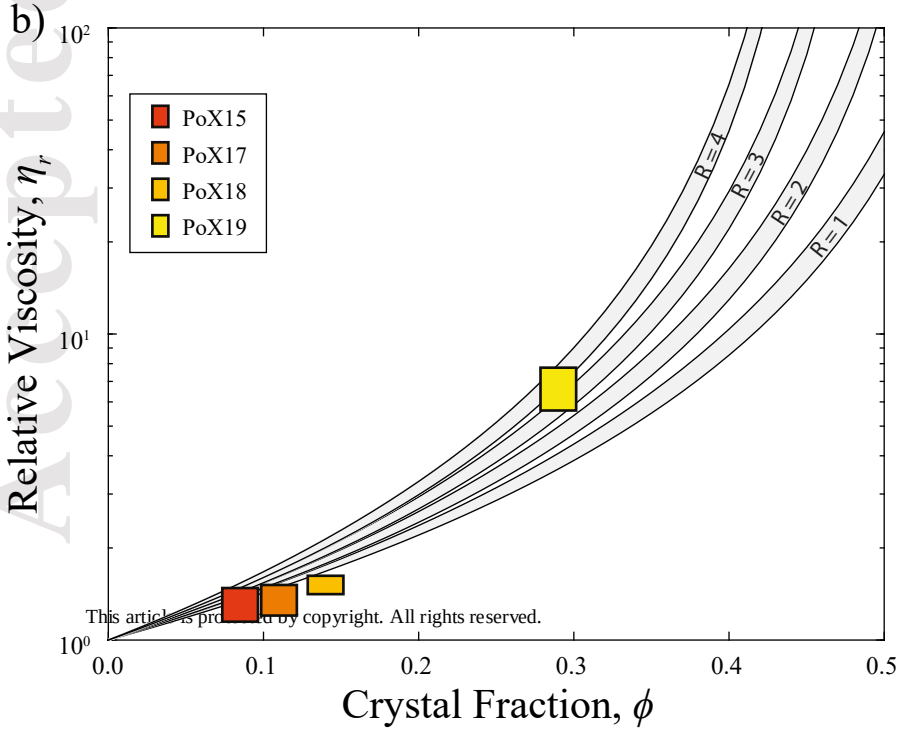

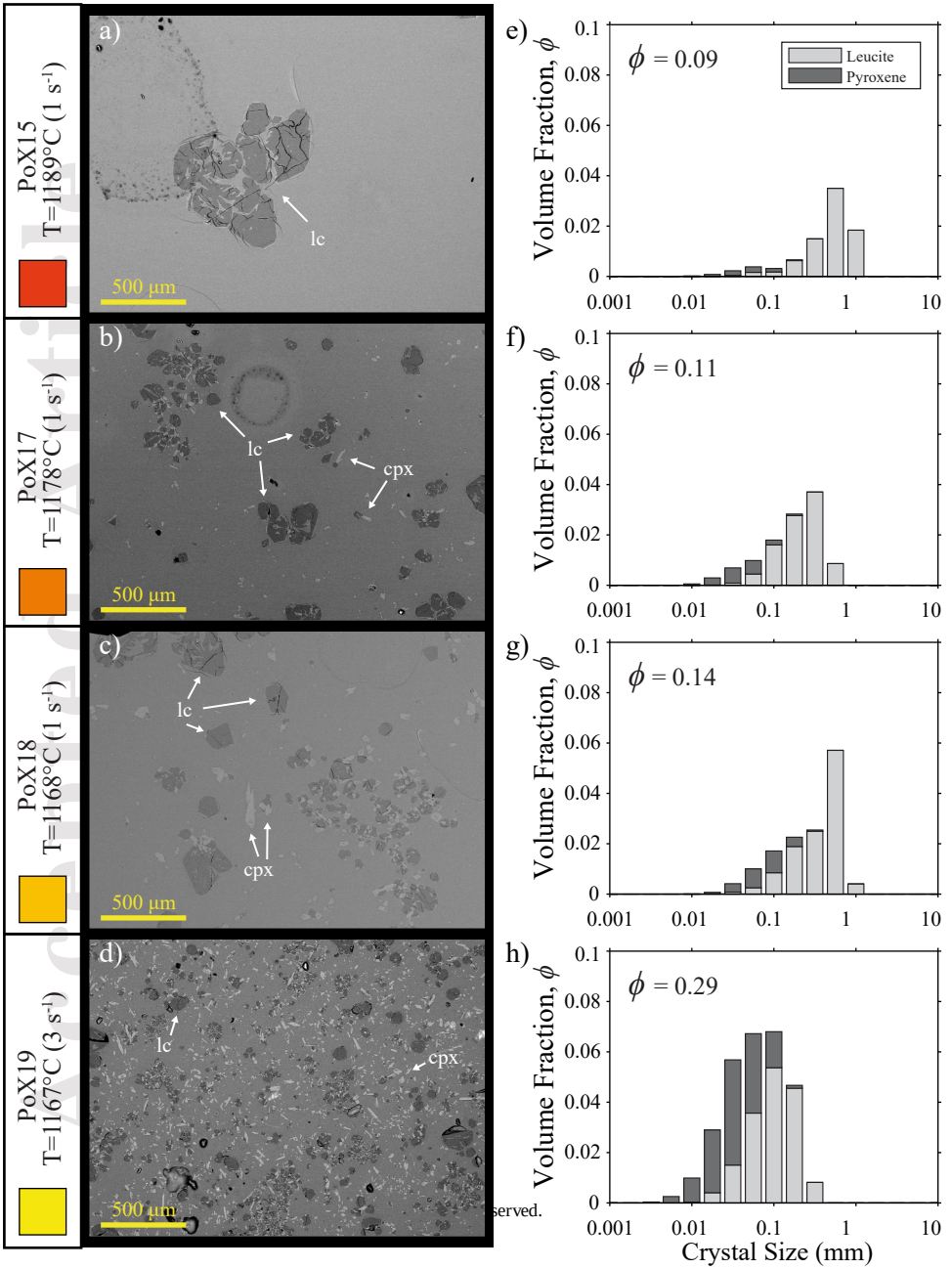
PoX15
T=1189°C (1 s-1)
PoX17
T=1178°C (1 s-1)
PoX18
T=1168°C (1 s-1)
PoX19
T=1167°C (3 s-1)
a)
b)
c)
d)
lc
cpx
500 µm
e)
f)
g)
h)
ϕ = 0.09
ϕ = 0.11
ϕ = 0.14
ϕ = 0.29
Leucite
Pyroxene
Volume Fraction, ϕ
0
0.02
0.04
0.06
0.08
0.1
0.001
0.01
0.1
1
10
Crystal Size (mm)

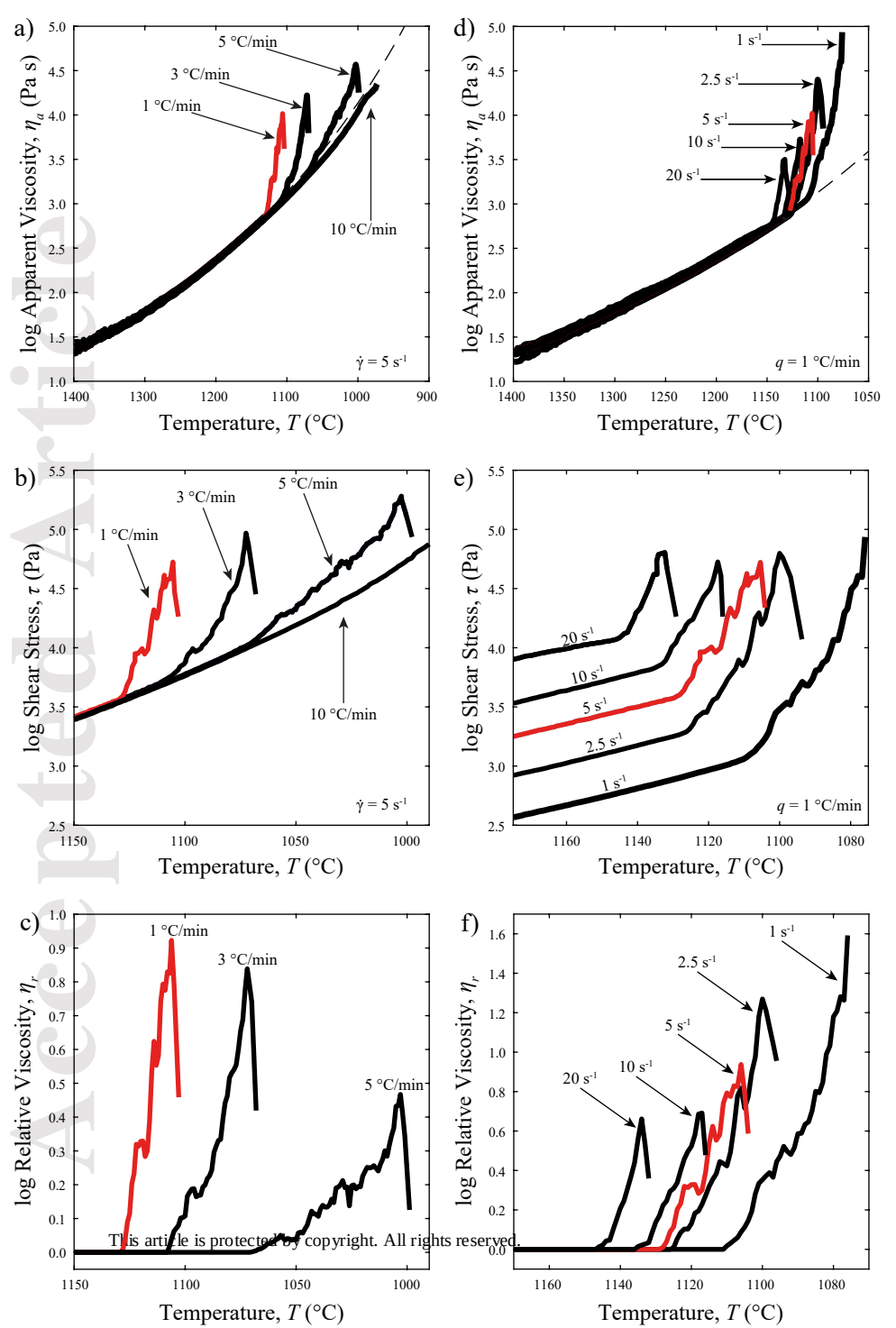

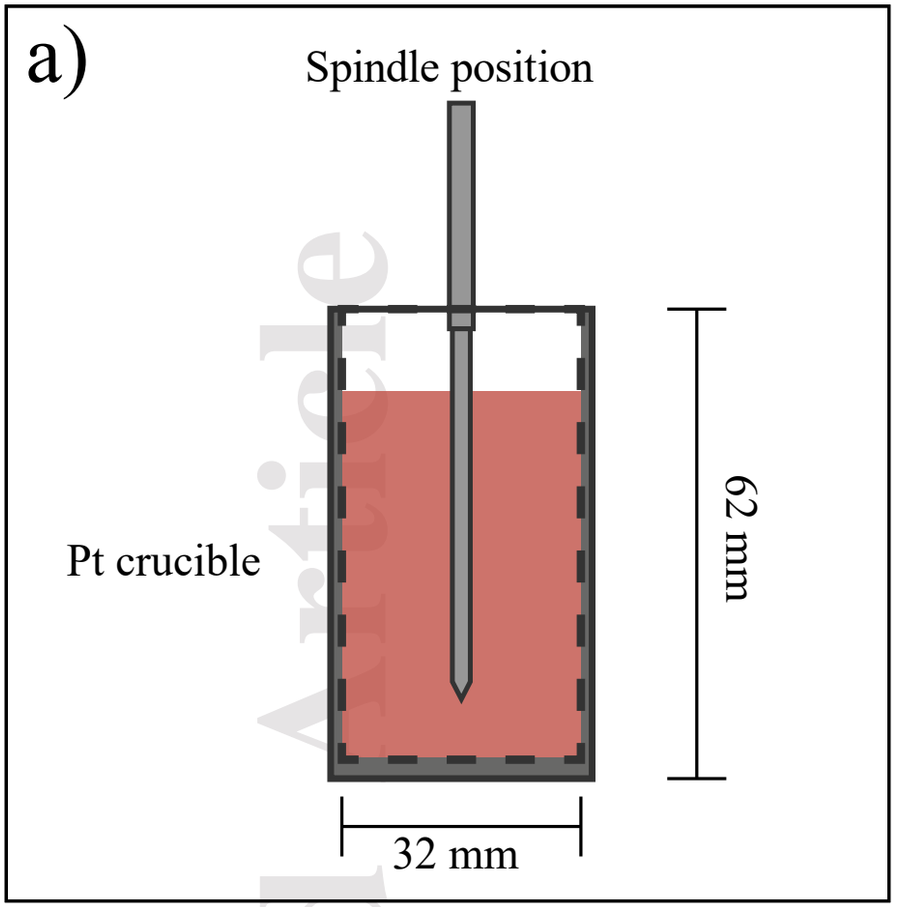

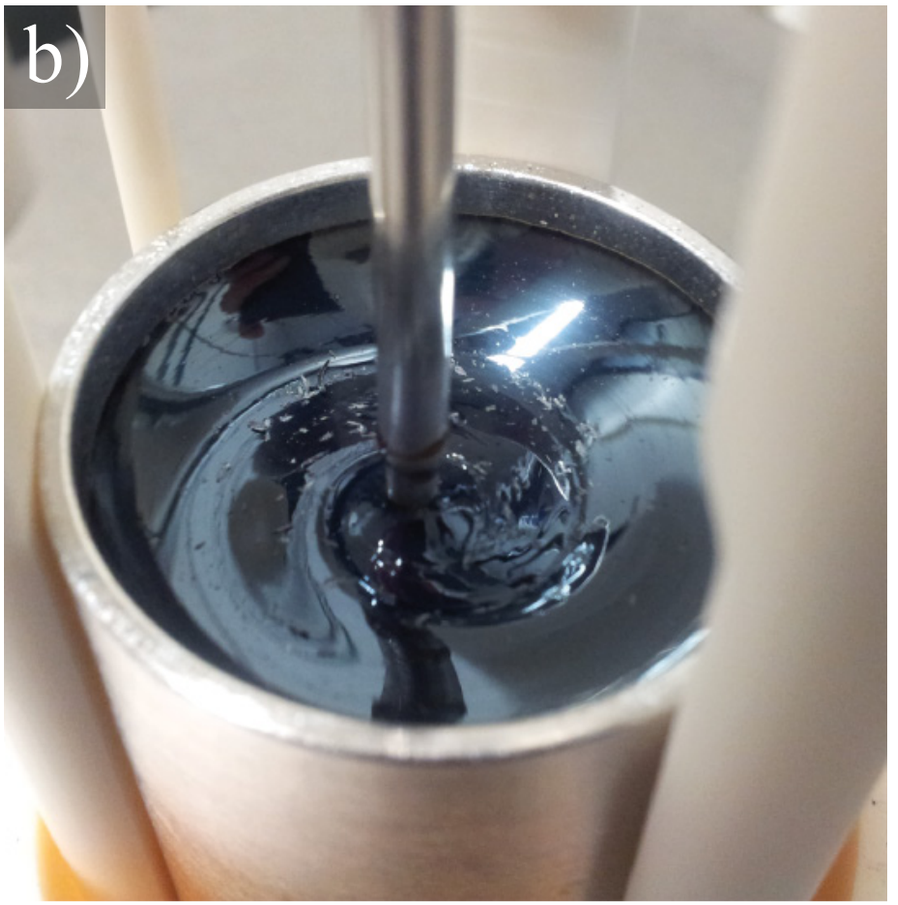

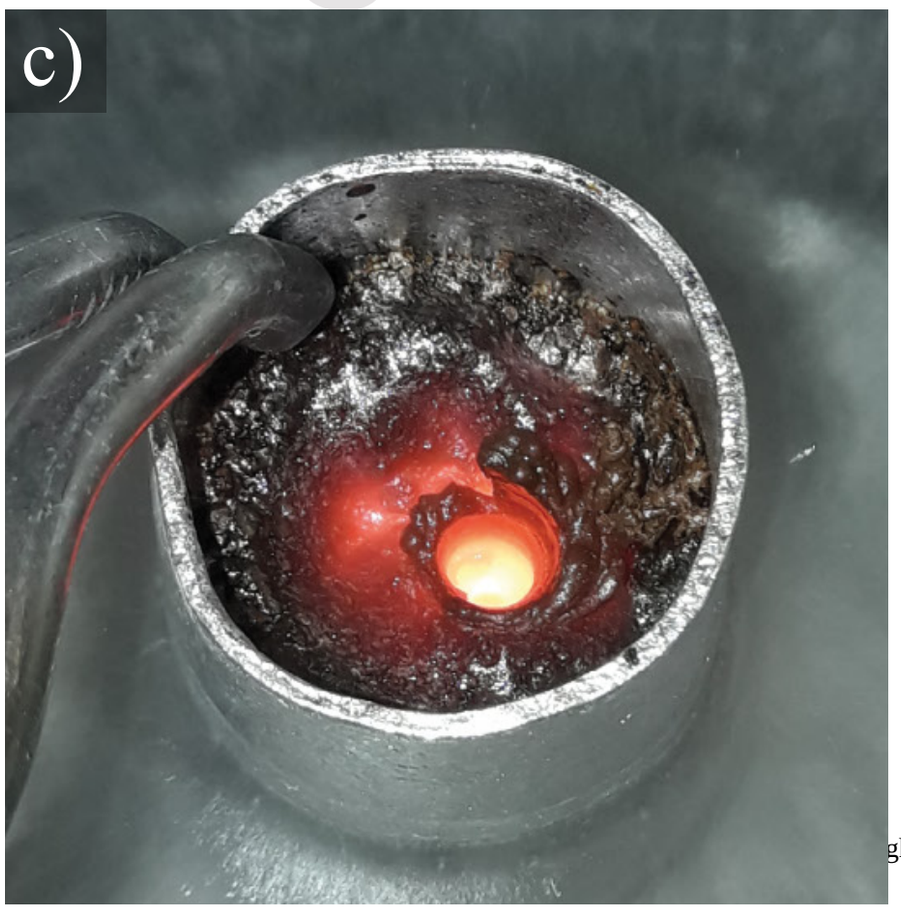

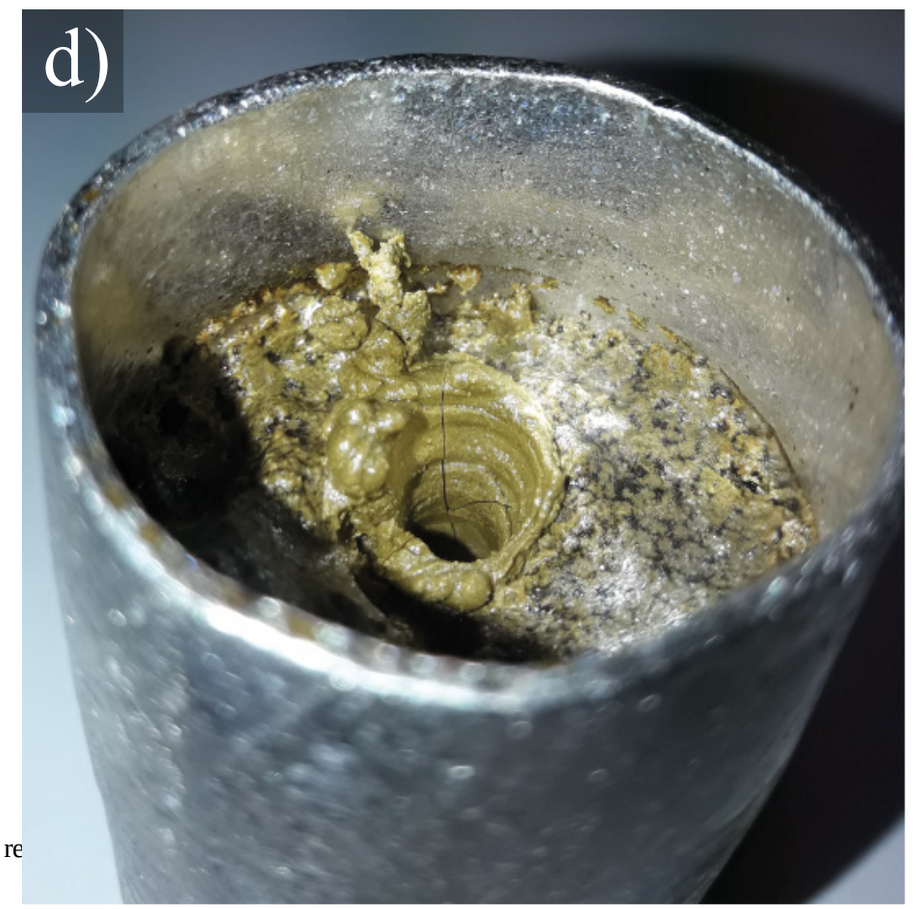

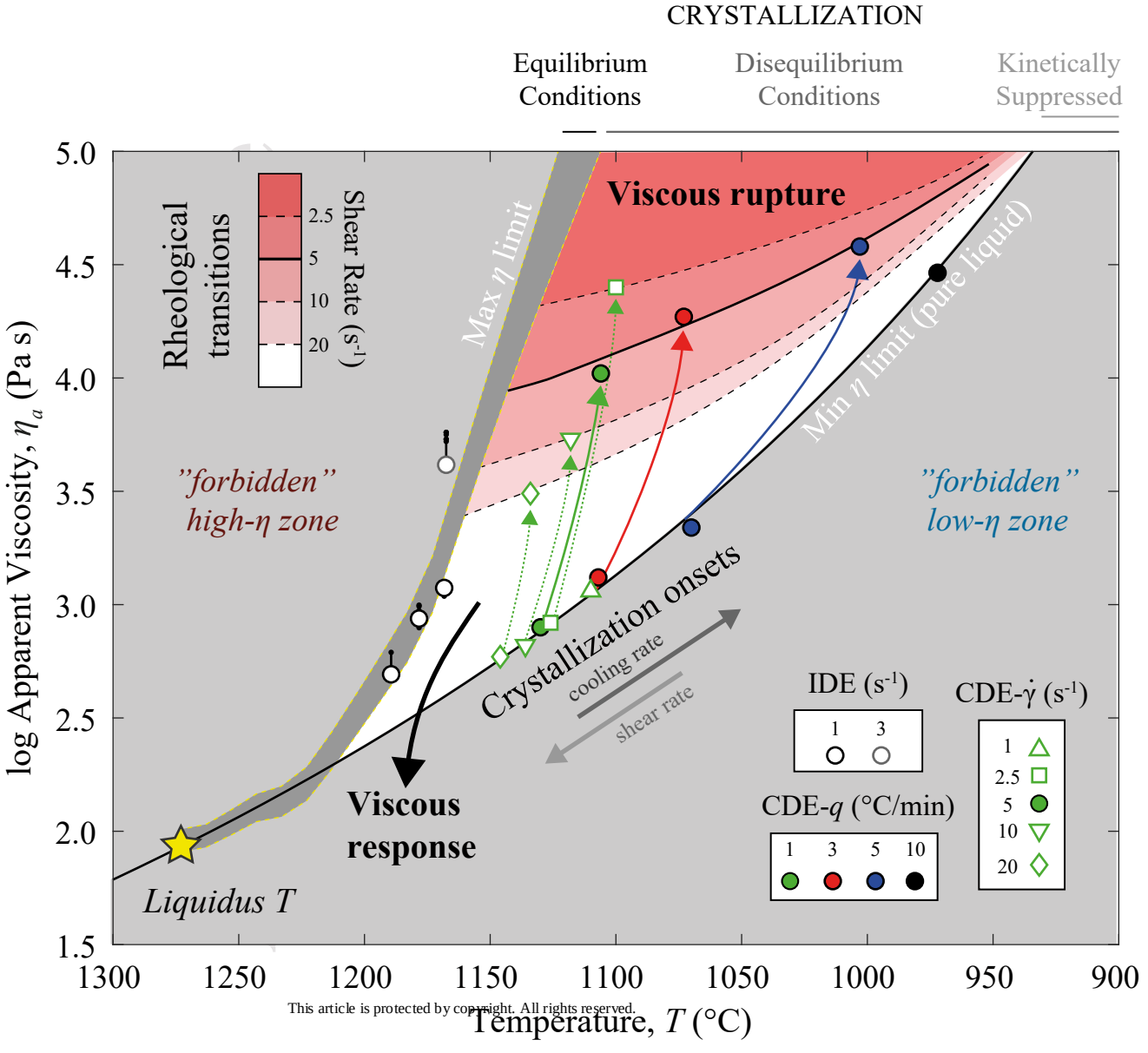

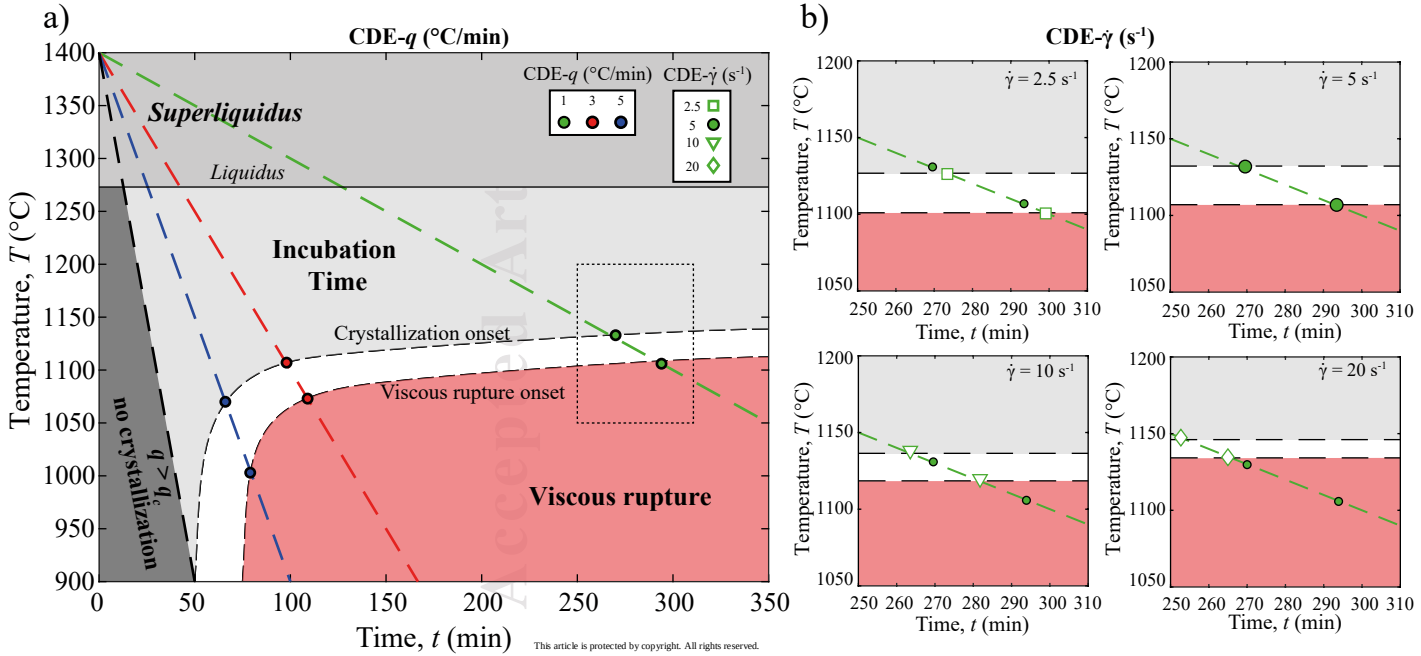

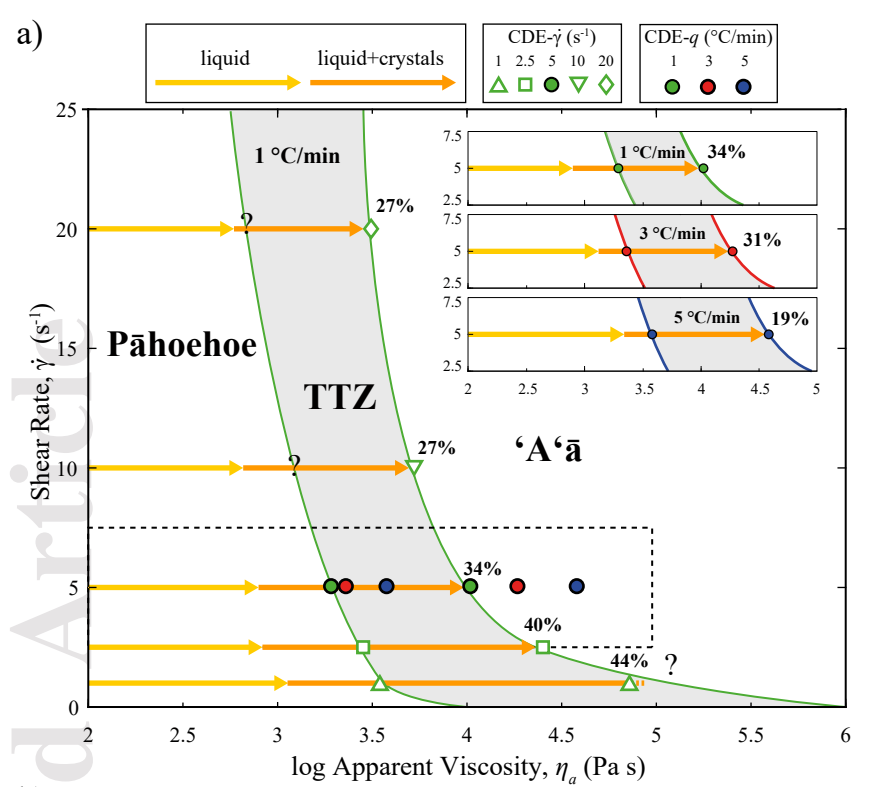

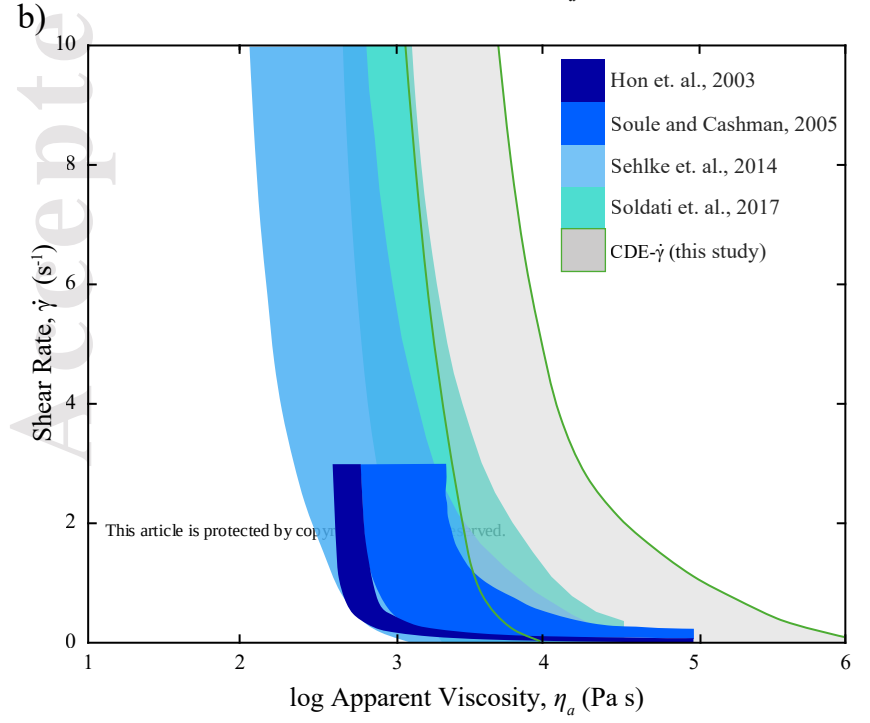

a)

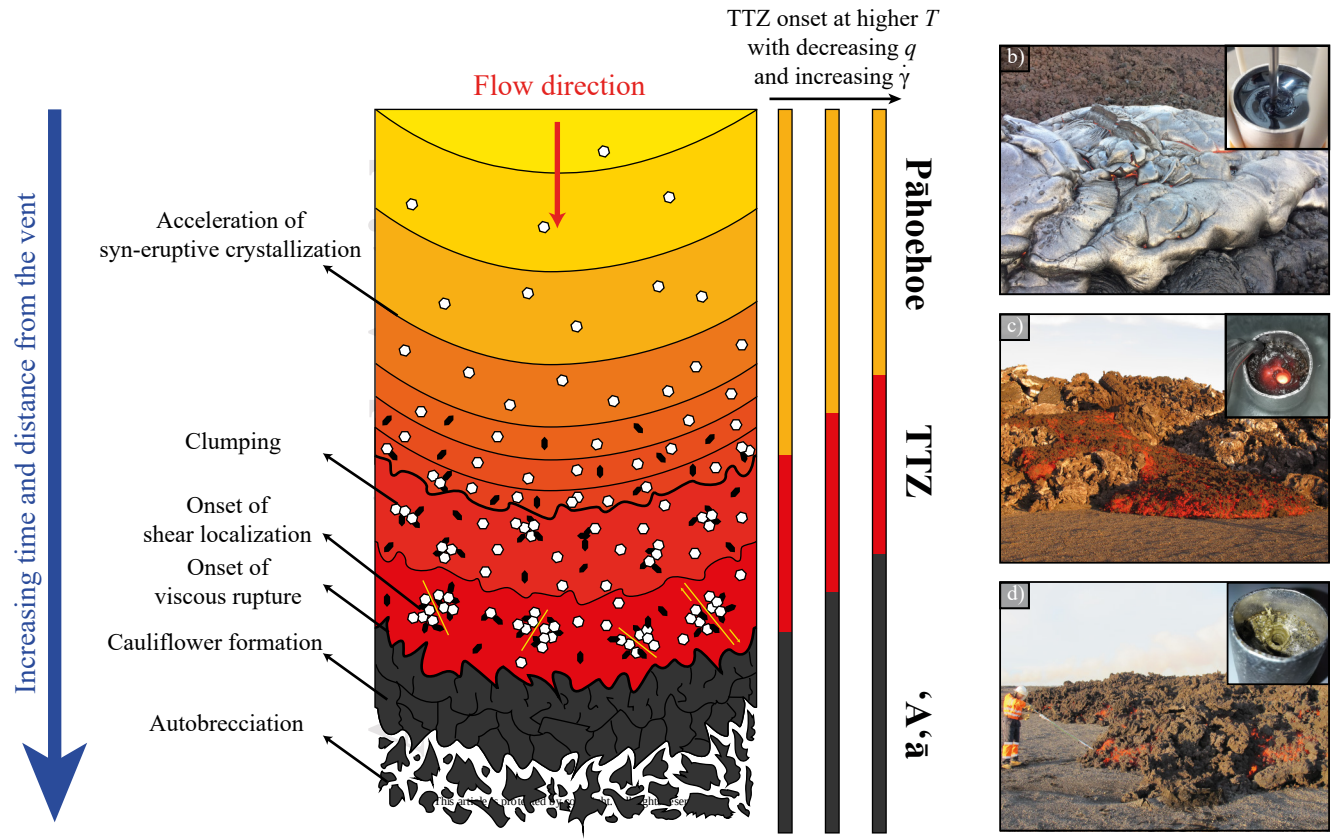
TTZ onset at higher T
with decreasing q
and increasing $\dot{\gamma}$
Flow direction
Increasing time and distance from the vent
Acceleration of
syn-eruptive crystallization
Clumping
Onset of
shear localization
Onset of
viscous rupture
Cauliflower formation
Autobrecciation
Pāhoehoe
TTZ
'A'ā
b)
c)
d)

Table 1 Notation of all variables.

Variable	Unit	Definition
t	s-min-h	Time
t_{inc}	min	Incubation time
t_{dep}	min	Time to reach rheological departure
t_{eq}	min	Time to achieve thermodynamic equilibrium
t_{vr}	min	Time to reach viscous rupture behavior
T	°C	Temperature
$T_{superliquidus}$	°C	*Superliquidus* temperature
$T_{liquidus}$	°C	*Liquidus* temperature (from thermodynamic modeling)
$T_{subliquidus}$	°C	*Subliquidus* temperature
T_{dep}	°C	Temperature of rheological departure
T_{onset}	°C	Temperature of crystallization onset
T_{vr}	°C	Temperature of viscous rupture onset
ΔT	°C	Initial degree of undercooling ($\Delta T = T_{liquidus} - T_{subliquidus}$)
ΔT_{onset}	°C	Effective undercooling at the crystallization onset ($\Delta T_{onset} = T_{liquidus} - T_{onset}$)
q	°C/min	Cooling rate ($\Delta T/t$)
q_c	°C/min	Critical cooling rate
$\dot{\gamma}$	s^{-1}	Shear rate
τ	Pa	Shear stress
τ_{vr}	Pa	Shear stress peak at viscous rupture
η	Pa s	Viscosity
η_a	Pa s	Apparent viscosity
η_{liquid}	Pa s	Crystal-free melt viscosity
η_0	Pa s	Residual melt viscosity
η_{vr}	Pa s	Apparent viscosity at viscous rupture
η_r	-	Relative viscosity
$d\eta_r/dT$	$°C^{-1}$	Increase of relative viscosity as a function of temperature
$d\eta_r/dt$	min^{-1}	Increase of relative viscosity as a function of time
ϕ	-	Crystal fraction
R	-	Mean aspect ratio of particles

Table 2 Results of IDEs subliquidus viscosity measurements.

Exp. ID#		PoX15	PoX17	PoX18	PoX19
Temperature, T (°C)		1189	1178	1168	1167
Initial Shear Rate, $\dot{\gamma}$ (s^{-1})		1	1	1	3
Initial Melt viscosity, η_{liquid} [log (Pa s)]	(measured)[a]	2.55	2.61	2.70	2.72
Residual Melt Viscosity, η_0 [log (Pa s)]	(predicted)[b]	2.62	2.82	2.89	2.87
Apparent viscosity, η_a [log (Pa s)][c]	*(0.1 s^{-1})*	2.79	-	-	-
	(0.3 s^{-1})	-	3.00	3.10	3.76
	(0.5 s^{-1})	2.72	2.99	3.09	3.76
	(0.7 s^{-1})	-	2.97	3.08	3.75
	(1.0 s^{-1})	2.69	2.94	3.07	3.73
	(1.5 s^{-1})	-	-	-	3.73
	(2.0 s^{-1})	2.69	2.91	3.06	3.72
	(3.0 s^{-1})	2.69	2.90	3.04	3.62
Crystal fraction, ϕ	ϕ_{xls}	0.09	0.11	0.14	0.29
Leucite fraction, ϕ_{lc}	ϕ_{lc}	0.08	0.09	0.12	0.16
Pyroxene fraction, ϕ_{px}	ϕ_{px}	0.01	0.02	0.02	0.13
Mean aspect ratio, R		1.3	1.5	1.4	3.2

[a] Viscosity value before crystallization onset (see Fig. 2); [b] Calculated on chemical basis using GRD viscosity model and compositions in Table S2; [c] Measured at post-crystallization plateau and different shear rates (in parenthesis).

Table 3 Results of disequilibrium viscosity measurements of CDEs.

CDE-q

Shear Rate, $\dot{\gamma}$ (s^{-1})		5	5	5	5
Cooling Rate, q (°C/min)		1	3	5	10
Temperature, T (°C)	*c.o.*	1130	1107	1070	-
	v.r.	1106	1073	1003	-
Time, t (min)	*c.o.*	270	98	66	-
	v.r.	294	109	79	-
Apparent viscosity, η_a [log (Pa s)]	*c.o.*	2.9	3.12	3.34	-
	v.r.	4.02	4.27	4.58	-
Shear Stress, τ [log (Pa)]	*v.r.*	4.72	4.97	5.28	-
log Relative Viscosity, η_r	*v.r.*	0.94	0.84	0.47	-
Crystal fraction, ϕ	*v.r.*	0.34	0.31	0.19	-
		(± 0.04)	(±0.04)	(± 0.02)	-
Volumetric crystallization rate (cm^3/s)	*a.v.*	0.009	0.019	0.010	-

CDE-$\dot{\gamma}$

Shear Rate, $\dot{\gamma}$ (s^{-1})		1	2.5	5	10	20
Cooling Rate, q (°C/min)		1	1	1	1	1
Temperature, T (°C)	*c.o.*	1110	1126	1130	1136	1146
	v.r.	-	1100	1106	1118	1134
Time, t (min)	*c.o.*	290	274	270	264	254
	v.r.	-	300	294	282	266
Apparent viscosity, η_a [log (Pa s)]	*c.o.*	3.06	2.92	2.9	2.82	2.77
	v.r.	-	4.4	4.02	3.73	3.49
Shear Stress, τ [log (Pa)]	*v.r.*	-	4.8	4.72	4.73	4.79
log Relative Viscosity, η_r	*v.r.*	1.59	1.27	0.94	0.69	0.66
Crystal fraction, ϕ	*v.r.*	-	0.40	0.34	0.27	0.27
		-	(± 0.05)	(± 0.04)	(± 0.04)	(± 0.03)
Volumetric crystallization rate (cm^3/s)	*a.v.*	-	0.010	0.009	0.010	0.015

c.o. = crystallization onset; *v.r.* = viscous rupture; *a.v.* = average value.